

Gate-tunable negative differential resistance in multifunctional van der Waals heterostructure

Richa Mitra,^{*,†} Konstantina Iordanidou,^{‡,§} Naveen Shetty,[†] Md Anamul Hoque,[†]
 Anushree Datta,^{¶,||} Alexei Kalaboukhov,[†] Julia Wiktor,[‡] Sergey Kubatkin,[†] Saroj
 Prasad Dash,^{*,†} and Samuel Lara-Avila^{*,†,⊥}

[†]*Department of Microtechnology and Nanoscience, Chalmers University of Technology,
 SE-412 96 Gothenburg, Sweden*

[‡]*Department of Physics, Chalmers University of Technology, SE-412 96 Gothenburg,
 Sweden*

[¶]*Université Paris-Cité, CNRS, Laboratoire Matériaux et Phénomènes Quantiques, 75013,
 Paris, France*

[§]*Materials Physics-Oslo, SINTEF Industry, NO-0314 Oslo, Norway*

^{||}*Université Paris-Saclay, CNRS, Laboratoire de Physique des Solides, 91405, Orsay,
 France*

[⊥]*National Physical Laboratory, Hampton Road, Teddington TW11 0LW, United Kingdom*

* E-mail: richa@chalmers.se; saroj.dash@chalmers.se; samuel.lara@chalmers.se

Abstract

Two-dimensional (2D) semiconductors have emerged as leading candidates for the development of low-power and multifunctional computing applications, thanks to their qualities such as layer-dependent band gap tunability, high carrier mobility, and excellent electrostatic control. Here, we explore a pair of 2D semiconductors with broken-gap (Type III) band alignment and demonstrate a highly gate-tunable p-MoTe₂/n-SnS₂

heterojunction tunnel field-effect transistor with multifunctional behavior. Employing a dual-gated asymmetric device geometry, we unveil its functionality as both a forward and backward rectifying device. Consequently, we observe a highly gate-tunable negative differential resistance (NDR), with a gate-coupling efficiency of $\eta \simeq 0.5$ and a peak-to-valley ratio of ~ 3 down to 150K. By employing density functional theory and exploring the density of states, we determine that interband tunneling within the valence bands is the cause of the observed NDR characteristics. The combination of band-to-band tunneling and gate controllability of NDR signal open the pathway for realizing gate-tunable 2D material-based neuromorphic and energy-efficient electronics.

Introduction

The quest for enhanced computational power, energy efficiency, and data processing capabilities continues to fuel the demand for novel materials and computational paradigms.¹ Tunnel field-effect transistors (TFETs) emerge as an exciting candidate to realize the longstanding promise of energy-efficient computation. In TFETs, band-to-band-tunneling²⁻⁶ serves as the primary carrier injection mechanism, as opposed to the conventional thermal injection, allowing to circumvent inherent fundamental constraints of field-effect transistors (FETs). To mention, band-to-band tunnelling allows for sharper turn ON/OFF of transistors and reduce sub-threshold swing ($SS = \frac{d \log I_D}{dV_G}$) below the thermionic limit of $SS \sim 60 \text{ mVdec}^{-1}$ in FETs at room temperature (with I_D the source-drain current, and V_G the gate voltage). Additionally, a hallmark feature of TFETs is that they exhibit negative differential resistance⁶⁻¹² (NDR), opening avenues for the implementation of multi valued logic in emerging applications, including but not limited to artificial intelligence^{13,14} and neuromorphic computing.¹⁵

In recent years, two-dimensional (2D) materials¹⁶⁻²⁰ have been explored to boost the performance of TFETs and to circumvent challenges often encountered when implementing TFETs with bulk semiconductors: the absence of dangling bonds on 2D crystals ensures a pristine, bond-free surface, and allows for the creation of atomically clean and sharp inter-

faces in 2D van der Waals (vdW) heterostructures. Moreover, 2D material TFETs provide an edge over their 3D counterparts, as reduced screening in two dimensions facilitates better electrostatic control of devices. With the plethora of 2D materials available at our disposal, carefully selecting combinations of materials is an important task. A design rule is that selecting smaller bandgap material as source compared to larger bandgap material (type I or straddling band-gap alignment) facilitates the generation of a higher concentration of tunnelling carriers, which enables efficient tunnelling through the barrier from the source to the channel. A larger bandgap of the channel material helps in reducing the off-state leakage current and improving the on-off current ratio of the device. Several heterojunctions implemented following these prescriptions have been demonstrated.^{6,12,21–32} Recent theoretical works have sparked interest into unconventional pairs of 2D semiconductors^{33–35} having broken (Type III alignment) or nearly broken-gap band alignment, suitable for TFET operation, as it facilitates efficient band-to-band-tunneling, resulting in high on-state current, low subthreshold swing, reduced power consumption and potential for faster logic operations.

Here we explore one such unconventional pair of 2D semiconductors, hitherto not reported before, in the light of tunable broken-gap band alignment by combining a few layers of p-MoTe₂ and n-SnS₂ which is predicted to have a naturally broken gap band alignment.^{34–38} By careful contact engineering, we have been able to achieve high p-type doping in few-layer MoTe₂ which has bandgap around ≈ 0.9 eV and acts like a source material, whereas SnS₂ having higher electron affinity and larger bandgap (≈ 2.2 eV) working like the channel material. By employing a dual-gated device geometry using hexagonal Boron Nitride (hBN) as dielectric, we demonstrate multifunctional behaviour of the junction: a tunable forward to reverse rectifying behavior with gate voltage. We observe NDR which is highly gate-tunable^{25,39–42} at temperatures down to 150K. We estimate a gate-coupling efficiency of $\eta \simeq 0.5$ which indicates excellent electrostatic coupling of the top gate with the junction. Our first-principles calculations based on density functional theory (DFT) predicts MoTe₂ valence band (VB) edge to be almost aligned with the conduction band (CB) edge of SnS₂.

We further show that the tunneling current observed for our devices stems from VB-VB tunneling, limiting the peak-to-valley-current-ratio (PVCR) to ~ 3 . Such nearly broken-gap band alignment is imperative for realising TFETs and our observation of NDR confirms the DFT calculations.

Results and Discussion

We stack 2D material flakes into heterostructures using a polymer-based hot pick-up technique. After exfoliating the flakes onto Si/SiO₂ and identifying suitable ones, the polymer-based pick-up at elevated temperatures ensures residue-free interfaces, which is critical for device fabrication. To enhance the interface quality, we perform vacuum annealing followed by an atomic force microscopy (AFM) scan to ensure the high quality of the devices. We use Ti(5nm)/Au(60nm) and Pd(15nm)/Au(60nm) for SnS₂ and MoTe₂, respectively to make ohmic contacts. For the dual-gated geometry, hBN/MoTe₂/SnS₂/hBN stacks are fabricated by adding a hBN layer (≈ 20 nm) over the junction. We have fabricated at least 5 stacks according to the above mentioned process. However, we present data from one backgated device (D1) and two dual-gated devices (D2, D3). All the details about device fabrication are described in supplementary information (SI) section S1.

The device schematic and the optical microscopic image of a dual gated device D2 are shown in Fig. 1(a) and (b), respectively. We characterise the individual flakes using atomic force microscopy (AFM) and Raman spectroscopy. The AFM topography reveals that MoTe₂ and SnS₂ flakes are multilayer (in the range of 4-9 layers for the former one and 12-25 layers for the later, respectively as shown in the inset of Fig. 1(b)). Raman analysis shows typical modes for each layer present in the junction, with pronounced modes at 233 cm⁻¹ for MoTe₂ and at 315 cm⁻¹ for SnS₂ (full Raman analysis in SI section S2). The schematic of broken-gap band alignment of the few-layer MoTe₂/SnS₂ junction is presented in Fig. 1(c), showcasing band bending near the interface due to charge transfer (SI section S3). Fig. 1(d) shows

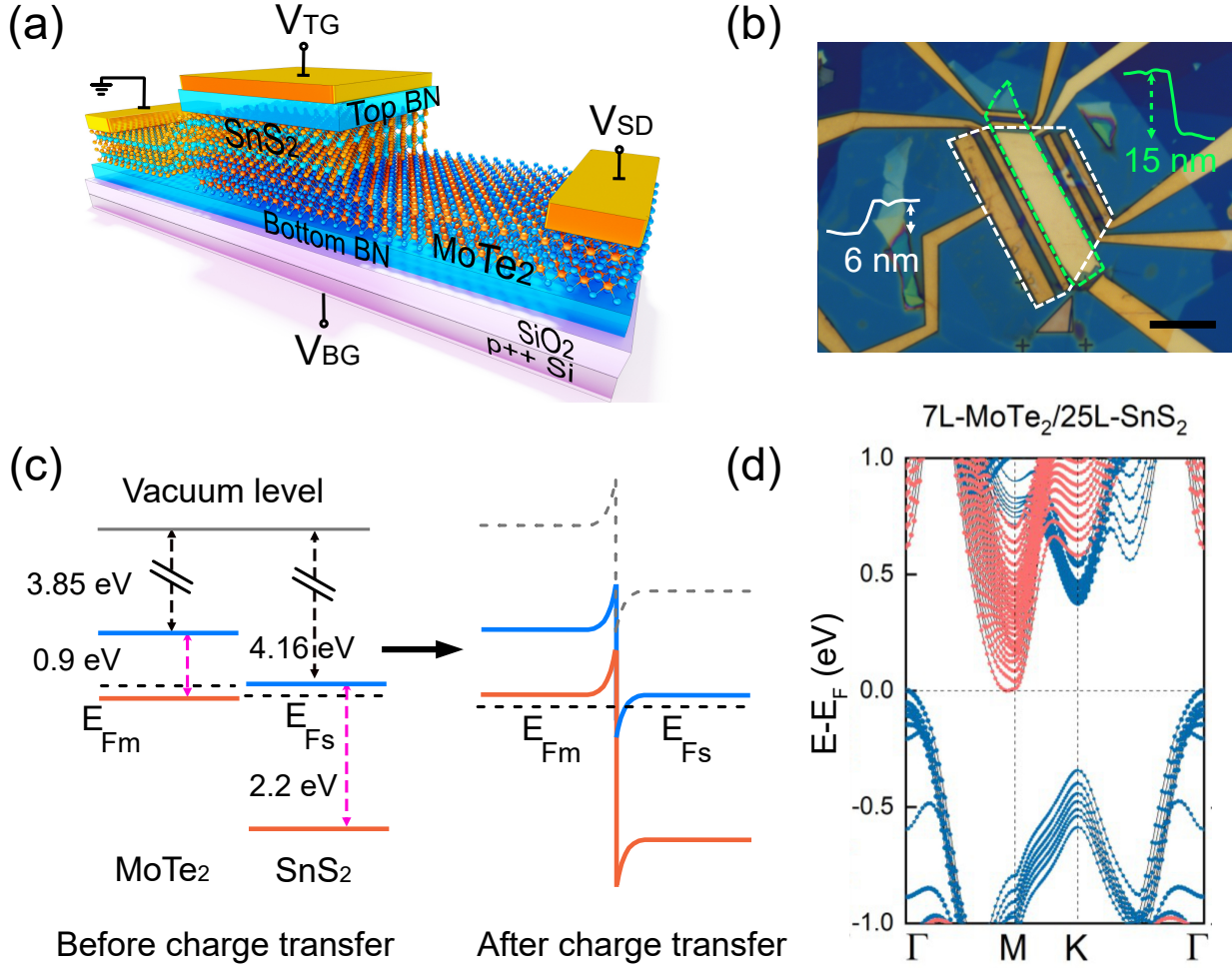


Figure 1: **Type III heterojunction with MoTe₂/SnS₂**: (a) Device schematic of a dual gated vertical heterojunction of MoTe₂ and SnS₂ on a Si/SiO₂ substrate. Metal contacts are deposited on the flakes and a topgate is defined over the junction with a thin hBN as the dielectric. Backgate V_{BG} and topgate voltages V_{TG} are applied across the SiO₂ substrate and top hBN respectively to change the carrier density. Biasing configuration is also shown where V_{SD} is applied to MoTe₂, SnS₂ is grounded. (b) Optical microscope image of the MoTe₂/SnS₂ junction (device D2). The scale bar corresponds to 10 μm . The white and green dashed region indicate boundaries of MoTe₂ and SnS₂ flakes respectively. The AFM height profiles of the individual flakes showing the flake thicknesses to be 6 nm and 15 nm corresponding to 9 and 25 layers respectively. (c) Broken-gap (type III) band alignment of MoTe₂ and SnS₂ before and after forming junction. The band bending appears as a result of charge transfer from MoTe₂ to SnS₂. (d) Band structure calculated using DFT calculations for 7-layer MoTe₂/25-layer SnS₂ heterojunction showing MoTe₂ VB maxima aligning with SnS₂ CB minima.

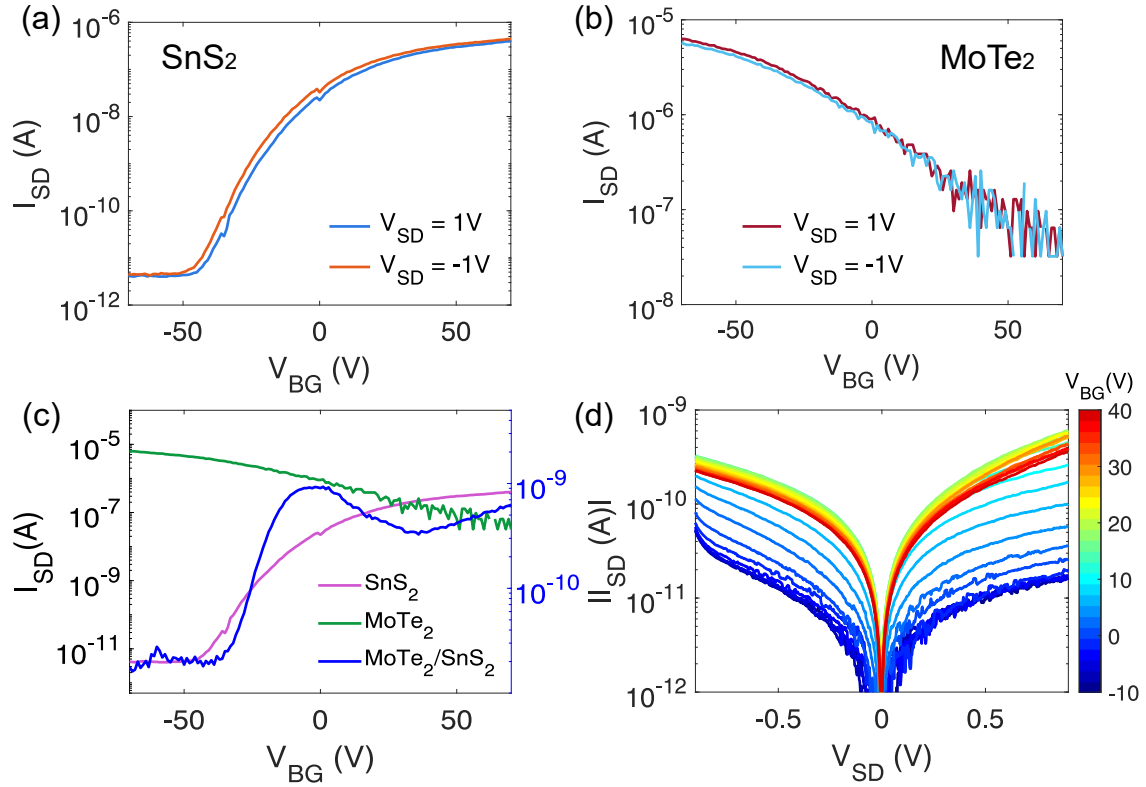


Figure 2: **Device characterisation from backgated device D1:** Transfer characteristic curves of SnS₂ (a) and MoTe₂ (b) measured at room temperature for $V_{SD} = \pm 1V$ and plotted in logarithmic scale for backgate voltages from -70V to 70V. (c) Transfer curves of the MoTe₂/SnS₂ junction (blue, right axis) plotted together with MoTe₂ (green, left axis), SnS₂ (pink, left axis) for $V_{SD} = 1V$. (d) Output characteristic i.e. I_{SD} vs. V_{SD} curves for the MoTe₂/SnS₂ junction for a range of backgate voltages (shown in colorbar) showing modulation of both forward and reverse bias current with V_{BG} .

the DFT computed band structure for a 7-layer MoTe₂/25-layer SnS₂ heterojunction. While Fig. 1(d) shows the DFT calculations for a specific combination of layer thickness, our calculations^{34,35} show that the broken gap alignment is a robust feature of the MoTe₂/SnS₂ heterostructure with different layer count (see SI section S10).

Backgated device

To understand the performance of the MoTe₂/SnS₂ junction, we first present the response of individual flakes for the backgated device D1 at room temperature. Fig. 2(a) and (b) show the transfer characteristics (source-drain current I_{SD} vs. backgate voltage V_{BG}) of SnS₂ and MoTe₂ flakes respectively at $V_{SD} = \pm 1V$ bias voltages. SnS₂ alone exhibits n-type FET behaviour with ~ 5 orders magnitude increase in current from OFF to ON state. In comparison, MoTe₂ shows p-type conduction with high current density, albeit less ON/OFF ratio, which we attribute to higher intrinsic doping of the MoTe₂ material. The corresponding curves for opposite bias voltages overlap and follow the same behavior, indicating formation of ohmic contact of the material with the contact (see also SI section S4 for linearity of IV curves). Next, we plot the transfer curves for individual flakes i.e. SnS₂, MoTe₂ (left axis) along with the junction (right axis) in Fig. 2(c). Depending on the backgate voltage, the junction creates a p/n density profile which results into the non-monotonic behavior of the junction current with backgate voltage. Fig. 2(d) depicts the output curves of the MoTe₂/SnS₂ junction in logarithmic scale for a range of backgate voltages. The source-drain current systematically increases with the range of V_{BG} for both positive and negative bias voltages. However, the backgate cannot systematically modify the band-alignment of the junction alone and thus the current flow in either bias configuration which prompts to implement dual gated devices.

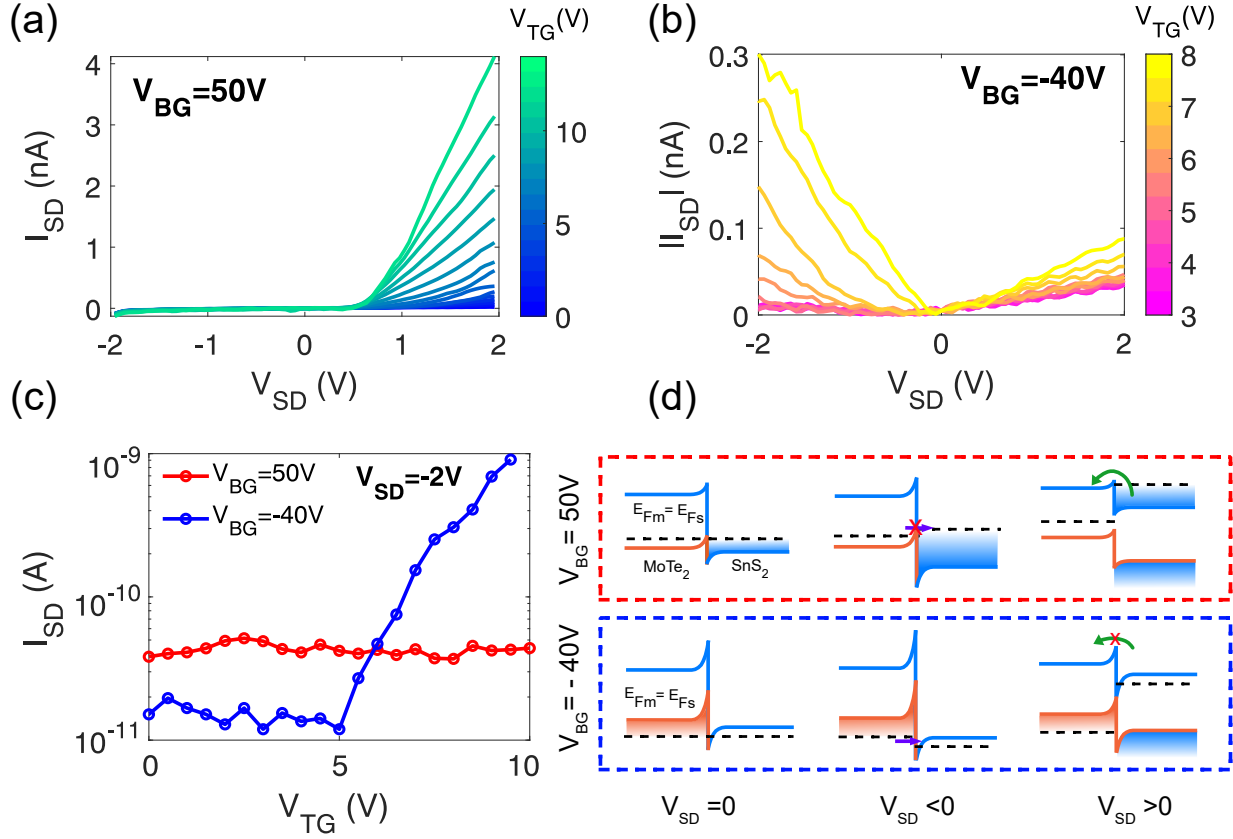


Figure 3: **Gate-dependant current rectification:** Output curves for opposite polarities of the back gate voltage (a) 50 V and (b) -40 V showing rectification at forward and reverse bias respectively. (c) Topgate response of the junction current at reverse bias ($V_{SD} = -2$ V) comparing rectification at -40 V to 50 V backgate voltage (Data for $V_{SD} = 2$ V in shown in SI section S5). (d) Band diagram at $V_{BG} = 50$ V (red box) and -40 V (blue box) showing different band alignment scenarios. Left panel shows equilibrium band alignment with $E_{Fm} = E_{Fs}$, reverse bias condition ($V_{SD} < 0$) in middle panel and forward bias condition ($V_{SD} > 0$) is shown in the right panel. Blue and orange lines indicate CB minima and VB maxima respectively for both materials. Orange and blue filled areas indicate hole filled states in MoTe_2 VB and electronic filled states in SnS_2 CB, respectively. The black dashed line signifies the local Fermi energies of the materials. States below Fermi energy are considered filled by electronic states. Larger band bending at zero bias for $V_{BG} = -40$ V is due to higher carrier density of MoTe_2 which determines the E_{Fm} and consequently E_{Fs} . At $V_{BG} = 50$ V, for high V_{TG} values, RB current is found negligible as electrons from MoTe_2 VB don not contribute to the junction current. However at $V_{BG} = -40$ V, charge carriers from MoTe_2 VB tunnel to empty DOS in SnS_2 CB which leads to finite current. Applying positive topgate changes SnS_2 density increasing the junction current.

Dual-gated device

To enhance the junction tunability, we implement a topgate with hBN as the dielectric. Data from dual-gated device D2 reveals multifunctional behaviour of the junction at opposite polarities of backgate voltages. Figure 3(a) and (b) demonstrate rectification of the junction current with topgate voltage in forward bias (FB) and reverse bias (RB) at opposite polarities of backgate voltage, respectively. Here output curves are plotted in linear scale for a range of V_{TG} , as indicated in the color bars. At positive backgate voltages, FB drain current increases significantly with rising V_{TG} , while RB current remains low and unaffected. Increasing topgate voltage changes the SnS₂ Fermi energy E_{Fs} to higher values, leading to an increase in source-drain current. In contrast, for a negative polarity of backgate voltage, current rectification is observed for negative polarities of source drain bias. Figure 3(c) summarizes the rectification behaviour by showing the change of source-drain current versus top gate voltage, at different polarities of the back gate voltage at $V_{\text{SD}} = -2\text{V}$ as shown in SI section S5.

In Fig. 3(d) we explain the bias effect observed in dual-gated device by sketching band alignment at different biasing and gating conditions. At zero bias, no current flows across the junction as the Fermi level is balanced across the junction. At RB, the SnS₂ band is lowered in energy and the band bending increases due to the in-built electric field. As a result, the total current is dominated by charge carrier tunnelling from the VB in MoTe₂ to the empty DOS in CB of SnS₂. At $V_{\text{BG}} = 50\text{V}$, MoTe₂ is depleted of p-type carriers. As a result, fewer carriers tunnel from the MoTe₂ VB to the SnS₂ CB, resulting in negligible RB current (indicated by a smaller purple arrow with a red cross). Now, applying a positive V_{TG} induces more charge carriers in SnS₂ which brings the E_{Fs} inside CB. However, due to lack of carriers present in MoTe₂, the junction current remains unaffected by the topgate voltage (indicated by the red plot in Fig. 3(c)). In contrast at $V_{\text{BG}} = -40\text{V}$, MoTe₂ is strongly p-doped which leads to: (a) E_{Fm} moving inside MoTe₂ VB, (b) E_{Fs} moving towards SnS₂ CB edge due to larger charge transfer and band bending. This band alignment leads to finite

RB tunneling current from MoTe₂ VB to SnS₂ CB (purple arrow). However with increasing topgate bias, E_{F_s} moves further inside the SnS₂ CB leading to significant increase in the RB current (blue plot in Fig. 3(c)). In summary, RB current rectification is dominated by carriers tunneling from MoTe₂ VB to SnS₂ CB. Topgate directly affecting SnS₂ DOS leads to higher current rectification when MoTe₂ is highly conducting i.e. at $V_{BG} = -40V$. Opposite scenario is observed in FB where the junction current mostly constitutes of thermionic current (green curved arrows in right panels in Fig. 3(d)). FB current depends on the initial band bending configuration and SnS₂ DOS, hence more tunable when MoTe₂ is depleted i.e. when $V_{BG} = 50V$ (SI section S5).

To further investigate on the carrier injection mechanism in FB and RB, we estimate the SS from the topgate response of the junction current. We calculate $SS \approx 700mV \text{ dec}^{-1}$ at $T=150K$ for $V_{SD} = 0.5V$ (SI section S6). The temperature dependence of the SS clearly indicate that, in FB condition thermionic injection and band-to-band-tunneling dominating the n and p-type transport, respectively.

Negative differential resistance

For our dual-gated devices we found that a suitable p^+-n^+ doping profile can be created for certain combinations of V_{BG} and V_{TG} , where the junction behaves like an Esaki diode.^{27,43,44} In Fig. 4(a), we present output curves for a range of V_{TG} voltages (indicated in the colorbar) at $V_{BG} = -10V$ (upper panel). We observe that, for each curve the FB current changes non-linearly with the bias voltage, namely increasing upto a certain bias ($= V_P$) and dropping down quickly and increasing again further for higher bias voltages. This behaviour known as negative differential resistance (NDR) to the applied top gate voltage in a wide range of V_{TG} values. As V_{TG} reduces from 0V, NDR peak appears at lower bias voltage, showing systematic reduction in V_P . We also observe orderly change in the peak current ($= I_P$) with the application of topgate voltage. Similar gate-tunable features of NDR are observed for $V_{BG} = -20V$ at $T= 150K$ (lower panel of Fig. 4(a)) and at $V_{BG} = -50V$, $T= 50K$ (SI

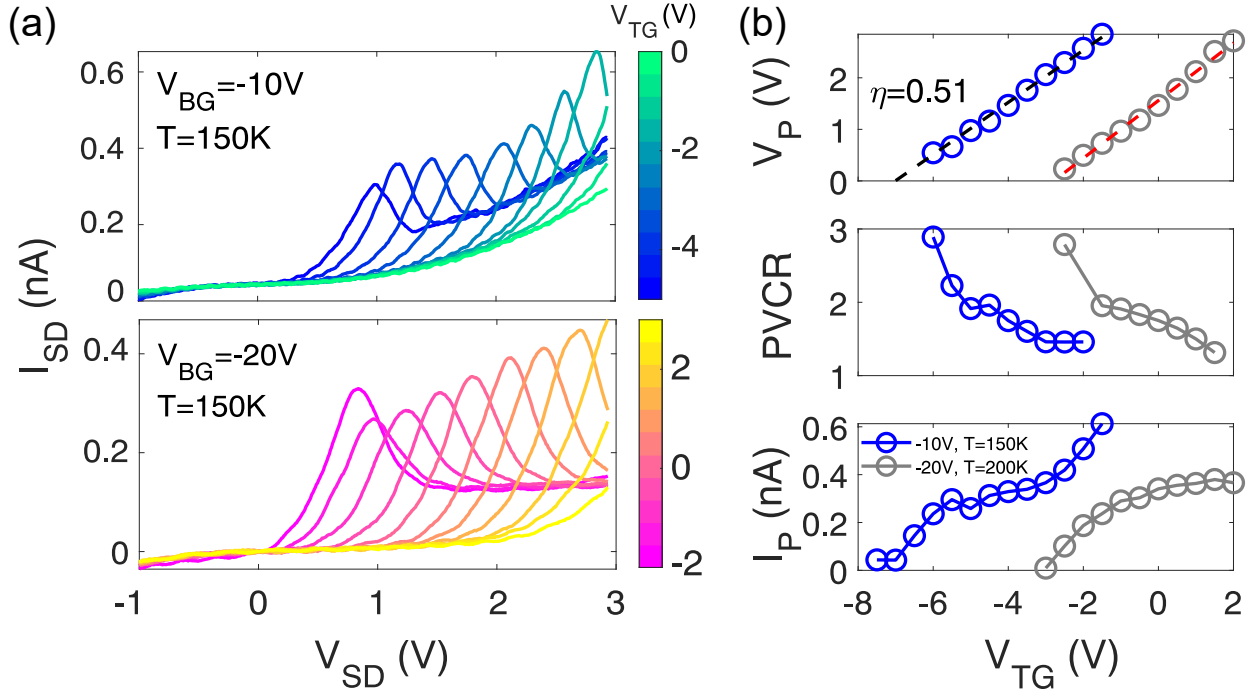


Figure 4: **Characterization of gate-tunable negative differential resistance in dual gated devices:** (a) Output curves of the dualgated device D2 showing NDR response at $V_{BG} = -10V$ (top panel), at $V_{BG} = -20V$ (bottom panel) measured at $T=150K$. Colorbars represent topgate voltages. (b) (top panel) V_P (bias voltage at which the NDR peak appears) vs. V_{TG} plot. Calculated slopes suggest the gating efficiency of $\eta = 0.51$. (Middle panel) Peak-to-valley current ratio ($PVCR = \frac{I_{Peak}}{I_{Valley}}$) vs. V_{TG} plot. (Bottom panel) Peak current I_P vs. V_{TG} . The blue and the gray circles (curves) represent data from device D2 measured at $V_{BG} = -10V$ at 150K and $V_{BG} = -20V$ at 200K, respectively.

section S7).

We now describe the characterization of the topgate tunable features of NDR. In the top panel of Fig. 4(b), we plot V_P as a function of the V_{TG} for two sets of gate-tunable NDR curves measured at $V_{BG} = -10V$, $T = 150K$ (blue circles) and at $V_{BG} = -20V$, $T = 200K$ (gray circles). We find V_P changing linearly with V_{TG} with a slope $\eta \approx 0.51$ (The black and red dashed lines) which refers to the gate-coupling efficiency of the topgate. Here gate coupling efficiency (η) is defined as the ratio of the change in V_P to the change in the topgate voltage. High η means that small changes in the gate voltage result in significant changes in moving the peak position, indicating strong gate control over the broken gap.

Figure 4(b) (middle panel) shows the top gate voltage (V_{TG}) dependence of the PVCR ($= \frac{I_{Peak}}{I_{Valley}}$), a key performance indicator of NDR devices. In our device, we find PVCR to be maximum $\sim 3 - 4$ at the lowest topgate values and reducing further as the topgate voltage increases. We provide a possible explanation for the NDR mechanism and PVCR values in the next section. Figure 4(b) (bottom panel) shows the I_P vs. V_{TG} plot for the similar V_{BG} and temperature combinations. We also observed NDR response in a separate dualgated device D3 (SI section S8) with a backgate-tunability feature. We found lower gating efficiency ($\eta \sim 0.2$) and a similar PVCR value.

We further characterised our TFET by estimating the inverse slope (IS), which is equal to the slope $\frac{\partial V_D}{\partial \log_{10} I_D}$ of the NDR curves. IS which is the measure of the current switching speed in NDR devices, is found to be as low as $600mV \text{ dec}^{-1}$ in our devices and can be tuned by the topgate voltage (SI section S9). Relatively higher values of IS in our devices can be attributed to the junction interface quality or device architecture. It can be improved by deliberately constructing smaller junctions and using stronger dielectric for better electrostatic control.

Theoretical interpretation

We carry out first-principles DFT calculations to understand gate-tunable NDR features of our devices, particularly the PVCR values in the heterojunction which is lower compared to

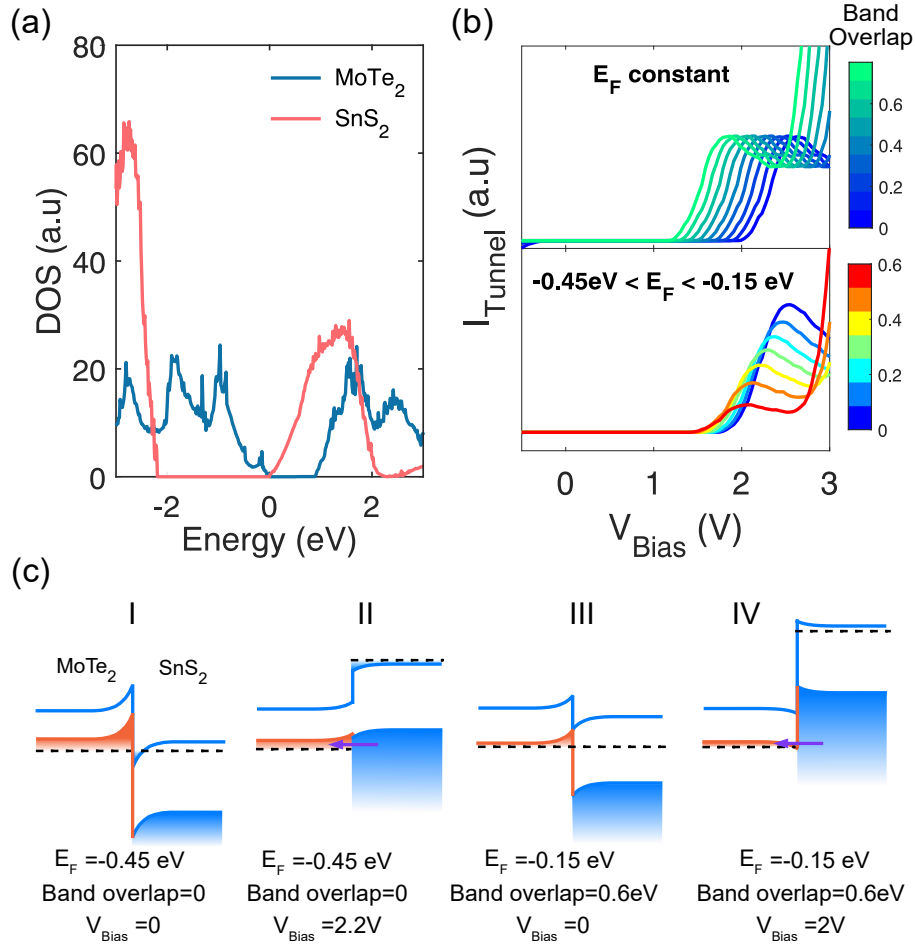


Figure 5: **Theoretical interpretation of NDR gate tunability:** (a) Partial density of states of MoTe_2 and SnS_2 from DFT. (b) Tunnel current (I_{Tunnel}) calculated from equation S4 using DFT DOS, plotted w.r.t bias voltage (V_{Bias}). I_{Tunnel} are estimated using DFT DOS for different band alignment configurations: (Upper panel) changing the band overlap i.e. the broken gap (indicated in colorbar in the units of eV) while keeping the Fermi energies constant ($E_{\text{Fm}} = E_{\text{Fs}} = -2$ eV). V_{peak} systematically changes while the I_{Tunnel} magnitude remains same. (Bottom panel) Changing the Fermi energies (-0.45 eV $< E_{\text{F}} < -0.15$ eV) along with changing the band overlap systematically modifies the magnitude of I_{Tunnel} along with NDR peak moving towards higher bias. (c) Schematic showing band alignment at different conditions of Fermi energy, band overlap and bias voltage. Blue and the orange curves outlines the CB and VB of both the materials and the black dashed line indicates the Fermi levels across the junction. Orange and blue filled areas indicate hole filled states in MoTe_2 VB and electronic filled states in SnS_2 CB, respectively. (From left to right) I and III panels show equilibrium band alignment for $E_{\text{F}} = -0.45$ eV with zero band overlap and for $E_{\text{F}} = -0.15$ eV with 0.6 eV band overlap. Schematic of the band alignment for configurations of I and III are shown in panel II and IV respectively for 2.2 eV and 2 eV forward bias voltage. The purple arrows indicate VB-VB tunneling contributing to the current. The direction of the arrays represent current carried by holes.

heterojunctions with other 2D materials reported in literature.^{12,45} In our devices, PVCR reduces with increasing V_{TG} which can be attributed to E_{Fs} moving closer to the CB minima of SnS_2 . Additionally, increase in the SnS_2 DOS with V_{TG} contributes towards higher thermionic current, which in turn increases the valley current and reduces the PVCR.

Our DFT calculations show the VB edge of MoTe_2 to be nearly aligned with the CB edge of SnS_2 for a range of 2D material thicknesses (SI section S10). Figure 1(d) demonstrated the band alignment for 7-layer MoTe_2 /25-layer SnS_2 , comparable with our measured device D2. We further utilise the partial DOS of MoTe_2 and SnS_2 to calculate the tunneling current according to the following expression:⁷

$$I_{\text{Tunnel}} = \int_{E_{\text{Fm}}}^{E_{\text{Fs}}} \text{DOS}_{\text{MoTe}_2}(E) \times \text{DOS}_{\text{SnS}_2}(E - eV_{\text{Bias}}) \times [f_{\text{MoTe}_2}(E) - f_{\text{SnS}_2}(E - eV_{\text{Bias}})] dE \quad (1)$$

Here $\text{DOS}_{\text{MoTe}_2}$ ($\text{DOS}_{\text{SnS}_2}$) and f_{MoTe_2} (f_{SnS_2}) represent the DOS and the Fermi distribution function of MoTe_2 (SnS_2) respectively. In Fig. 5(a) we plot the partial DOS of the two materials with zero ‘band overlap’ implying the VB maxima of MoTe_2 aligns with CB minima of SnS_2 at Energy = 0. We define negative (positive) ‘band overlap’ to the band alignment when SnS_2 CB minima is lower (higher) in energy than VB maxima of MoTe_2 . We also retain the usual convention that positive (negative) V_{Bias} shifts the SnS_2 bands towards higher (lower) energy with respect to the MoTe_2 bands. In Fig. 5(b), we plot the theoretically estimated tunneling current (I_{Tunnel}) as a function of the bias voltage (V_{Bias}) for two different configurations of band alignment. The upper panel refers to a situation when Fermi energies remain constant ($E_{\text{Fm}} = E_{\text{Fs}} = -2$ eV in this case) while the band overlap changes from 0 to 0.7 eV (indicated by the color bars). We found the NDR peak moving to lower V_{Bias} with increasing band overlap as expected. However, we observe that if E_{Fs} changes systematically with the band overlap, the peak current increases in magnitude along with the peak position, as shown in the bottom panel of Fig. 5(b).

To superimpose the above mentioned scenario to our measured devices, we conjecture that

the topgate electric field leads to such change in E_{Fs} along with tuning the band overlap. As a consequence of finite $\text{DOS}_{\text{SnS}_2}$, reducing V_{TG} can affect the band alignment in two ways: (a) the topgate electric field reduces the band overlap and (b) it depletes SnS_2 which is reflected as E_{Fs} moving towards the SnS_2 bandgap. For $V_{\text{BG}} = -10\text{V}$ and -20V (Fig. 4(a)), the topgate effectively changes both E_{Fs} and the band overlap, hence we observed gate-tunable V_{P} and I_{P} . However, at $V_{\text{BG}} = -50\text{V}$, I_{P} does not change, only the V_{P} gets affected by topgate. We believe at $V_{\text{BG}} = -50\text{V}$ the topgate primarily influences the band overlap, attributed to the reduced effect of backgate electric field on E_{Fs} influenced by charge carrier screening of bottom MoTe_2 . This results in higher carrier density in SnS_2 where the topgate's electric field is less effective in tuning E_{Fs} . Additionally, our analysis show that the gate-tunability of I_{Tunnel} which directly reflect changes in band overlap, is predominantly governed by VB-VB tunneling (SI section S11). In Fig. 5(c), we sketch possible band alignment at different conditions of Fermi energies, band overlap and bias voltages. Panel I and III show equilibrium band alignment (i.e. $V_{\text{Bias}} = 0$) with band overlap=0, $E_{\text{F}} = -0.45$ eV and for band overlap=0.6 eV, $E_{\text{F}} = -0.15$ eV respectively. Panel II and IV show band alignment at forward bias of 2.2 eV and 2 eV respectively. For high enough V_{Bias} , SnS_2 bands are pushed upwards in energy. As a result, the current mostly consists of charge carriers tunneling from SnS_2 VB to MoTe_2 VB (indicated by the purple arrow). The band overlap being higher in panel III, it leads to contribution from tunneling current as well. The effects of different configuration of band overlap and Fermi energies are demonstrated in SI section S11 by sketching the DFT DOS directly.

Conclusion

In conclusion, we demonstrated a multifunctional dual-gated vdW heterojunction by combining a few layers of MoTe_2 and SnS_2 . The junction exhibits high backgate-tunability, transitioning from a forward rectifying to a reverse rectifying diode at extreme backgate voltages, with a rectification ratio exceeding two orders of magnitude. Our devices demonstrate Esaki

diode behavior, exhibiting negative differential resistance at temperatures as high as 200 K. The NDR curves exhibit excellent tunability with the topgate voltage, achieving a gating efficiency of approximately 0.5 and a peak-to-valley-current ratio i.e. $PVCR \sim 3$ at 150K. Utilizing DFT calculations, we estimate the tunneling current, identifying conduction band-to-conduction band tunneling as the dominant contribution. We attribute the gate-tunable features of the NDR curves to a combined effect of band overlap and Fermi energy tuning induced by the topgate. The strong gate controllability of NDR indicates efficient manipulation of the broken gap band alignment in our devices. Our findings underscore NDR as a valuable tool for probing broken gap band alignment in such junctions and emphasize the importance of material selection and effective gate-tunability for achieving specific band alignments in 2D material-based devices.

Acknowledgement

The authors acknowledge financial support from the 2D TECH VINNOVA Competence Center (No. 2019-00068), the FlagEra projects H2O and MagicTune (funded by VR), the European Union Graphene Flagship project 2D Materials of Future 2DSPIN-TECH (No. 101135853), and the Graphene Center, AoA Nano, AoA Materials, and AoA Energy programs at Chalmers University of Technology. J.W. acknowledges funding from the Swedish Strategic Research Foundation through a Future Research Leader program (FFL21-0129). This work was performed in part at Myfab Chalmers and the Chalmers Materials Analysis Laboratory (CMAL).

Methods

We fabricate the heterojunctions using a standard exfoliation and 2D material stacking process. MoTe_2 , SnS_2 , and hBN crystals are exfoliated using blue Nitto tape or Scotch tape over small pieces of PDMS sheets. Suitable flakes of the materials are identified and selected

under an optical microscope. Using a micro-manipulator equipped with x, y, and z precision stages, as well as rotation and heater configurations, we transfer hBN, MoTe₂, and SnS₂ onto Si/SiO₂ substrates in that order. After the stacking process, the devices are vacuum annealed at 120°C for 2 hours at a pressure of approximately 2×10^{-6} mbar. This step helps achieve a residue-free interface.

For contact fabrication, the samples are spin-coated with a bilayer resist followed by e-beam lithography. The source and drain contacts are fabricated in a two-step process, where we pattern the contacts on MoTe₂ and SnS₂ flakes separately using e-beam lithography, followed by e-gun evaporation of metal and liftoff in hot acetone. We use Pd/Au (15 nm/70 nm) and Ti/Au (15 nm/70 nm) as the metal combinations for MoTe₂ and SnS₂, respectively. For dual-gated devices, we transfer another hBN layer on top of the junction and define the top gate using a similar patterning process.

All samples are wire-bonded and loaded into a 4K wet cryostat for characterization and measurement. We use a variable gain current amplifier, FEMTO DHPA-100, for applying biasing voltage and current measurement, and a Keithley 2400 for backgating and topgating purposes.

Supplementary Information

S1. Device fabrication

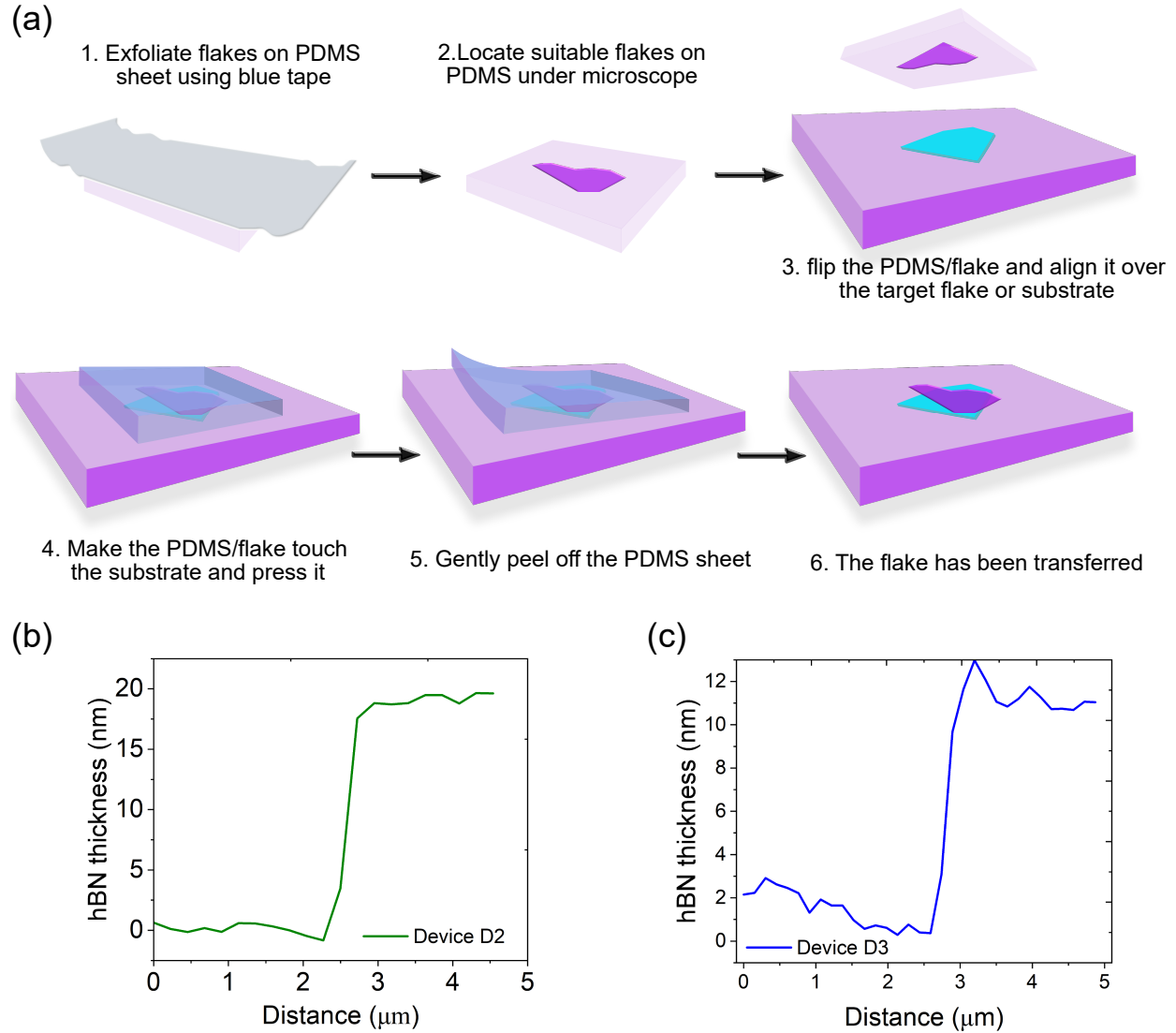


Figure S1: **Device fabrication:** (a) Step by step process for 2D material exfoliation and dry transfer method. AFM height measurement of top hBN used as the topgate dielectric in device (b) D2 and (c) D3.

In this section, we describe the steps of device fabrication which involves exfoliation and stacking of hexagonal boron nitride (hBN), MoTe₂ and SnS₂, followed by fabrication of electrical contacts and topgate probes. We start by exfoliating thin flakes of MoTe₂, SnS₂ and

hBN from their respective bulk crystals using blue nitto tape or scotch tape. The exfoliated flakes are transferred from the tapes to separate PDMS sheets (we cut 4mmx 4mm pieces of PDMS and stick them on transparent glass slides). Flakes with suitable shapes and thicknesses of different material are identified under the optical microscope carefully. After identifying suitable hBN, MoTe₂ and SnS₂ flakes under optical microscope, they are sequentially transferred onto a separate Si/SiO₂ substrate having predefined alignment markers. The substrates are always cleaned with hot acetone followed by IPA and baked at 120°C for 15 minutes to remove organic contaminants and to adsorbed water. We use a transfer setup equipped with x, y and z precision alignment and heating stage for assembling the stacks at ambient condition. The step by step procedure of exfoliation and dry transfer technique has been shown schematically in Fig. S1 (a). After stacking hBN/MoTe₂/SnS₂, we anneal the final stack inside a vacuum anneal chamber at 120°C for 2 hours at a pressure of $\sim 2 \times 10^{-6}$ mbar. Annealing aids removing any organic residues trapped inside the van der Waals layer which helps improving the interface quality.⁴⁶ After that, we spin coat the substrate with bilayer resist (Copolymer MMA/ARP) followed by baking the resist over hotplate at 150°C for 5 minutes. We pattern the source and drain contacts on MoTe₂ and SnS₂ flakes separately using e-beam lithography followed by e-gun evaporation of metal and liftoff. We use the metal combinations of Pd/Au (15nm/70nm) and Ti/Au (15nm/70nm) for MoTe₂ and SnS₂, respectively. We choose high work function Pd ($\Phi = 5.6\text{eV}$)^{47,48} which forms ohmic contact with MoTe₂ and helps efficient injection of p-type carriers into the channel. We find Titanium ($\Phi = 4.33\text{eV}$)⁴⁹ to be suitable for injecting electrons into SnS₂. Finally, liftoff is performed in the hot acetone to remove the excess metal. For the dual-gated devices, we further stack additional hBN to cover the junction area following the aforementioned dry transfer method. After that, a topgate is defined over the overlap junction of MoTe₂/SnS₂ by depositing Ti/Au (15nm/80nm). For topgate, we choose the hBN thickness to be $\sim 15 - 20$ nm as shown in Fig. S1 (b).

S2. Raman spectroscopy

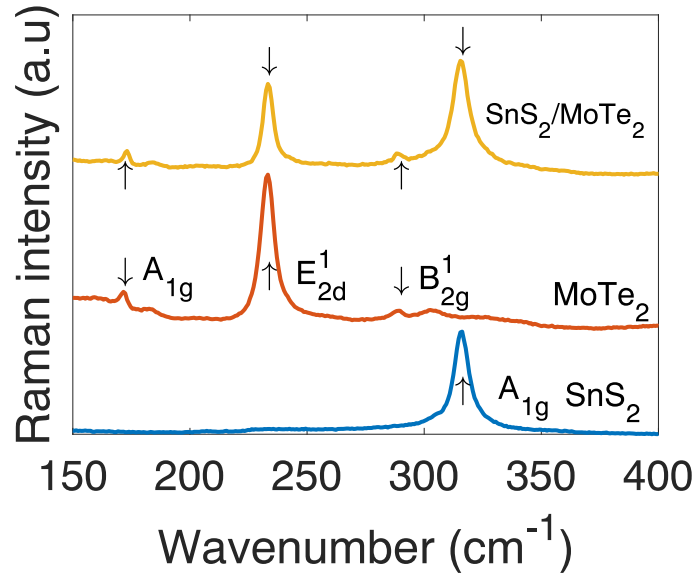


Figure S2: Raman spectra of MoTe₂, SnS₂ flakes and the MoTe₂/SnS₂ junction.

We used 532 nm laser source for acquiring the Raman signal of the individual flakes as well as the junction of the device as shown in Fig. S2. The Raman spectra shows the characteristic A_{1g} phonon modes of SnS₂⁵⁰ at 315 cm⁻¹. For MoTe₂,⁵¹ Raman peaks are observed at wave number 233 cm⁻¹, 173 cm⁻¹ and 289 cm⁻¹ which corresponds to the in-plane E_{2g}^1 , out-of-plane A_{1g} and B_{2g}^1 modes respectively. The MoTe₂/SnS₂ junction carries Raman signal for both the materials (indicated by arrows) as shown in the yellow curve.

S3. Work function calculation using Kelvin Probe Force Microscopy

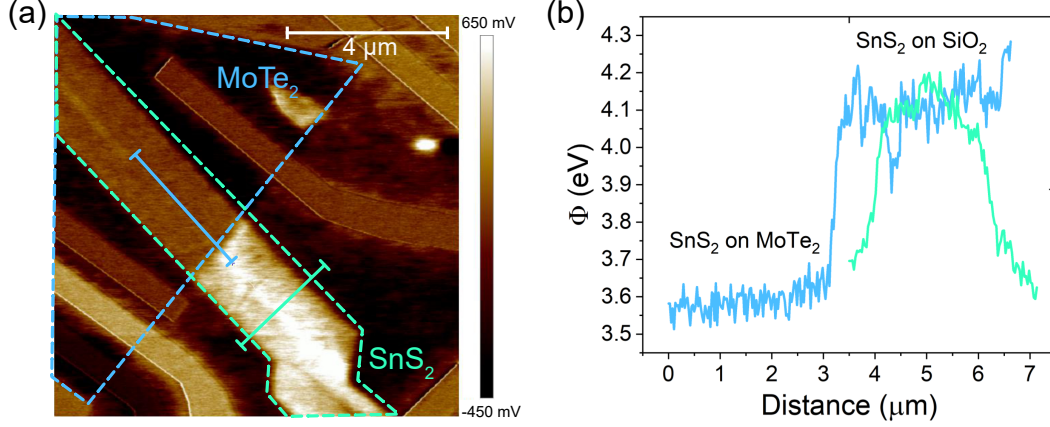


Figure S3: **KPFM measurement:** (a) 2D KPFM map of a MoTe₂/SnS₂ device. The scalebar corresponds to 4 μm length. The boundaries of the two materials are highlighted. (b) Calculated work function (Φ) from the 2D map with distance along the line (indicated in (a)) shows work function of SnS₂ over the MoTe₂ region is reduced than that on SiO₂ indicating charge transfer from SnS₂ to MoTe₂.

We use Kelvin probe force microscopy (KPFM) to probe the work function of the SnS₂, MoTe₂ and investigate the charge transfer across their heterojunction. In KPFM, one measures the contact potential difference (CPD) between the work functions of the tip (W_{tip}) and the surface/sample (W_{sample}):

$$V_{CPD} = \frac{(W_{\text{tip}} - W_{\text{sample}})}{e} \quad (\text{S1})$$

Here, e is the electronic charge. Therefore, in order to obtain the work function of the sample, we calibrated the work function of the tip. This is done by measuring on a known sample, such as oriented pyrolytic graphite (HOPG) ($W_{\text{HOPG}} = 4.48 \text{ eV}$):

$$W_{\text{tip}} = eV_{CPD} + W_{\text{HOPG}} = eV_{CPD} + 4.48V \quad (\text{S2})$$

By combining equations S1 and S2, one can calculate the work function of the unknown

sample. We found $V_{\text{CPD}} = 1\text{V}$ for our Platinum-Iridium coated tip with HOPG. Fig. S3 (a) shows 2D scan of voltage measured between the Kelvin probe tip and the flake for a $\text{MoTe}_2/\text{SnS}_2$ sample. We clearly see different contrast if the SnS_2 flake part on MoTe_2 and on SiO_2 substrate. Fig. S3 (b) shows the work function (Φ) plotted as a function of distance along two lines indicated in Fig. S3 (a). We find Φ to be $\sim 4.2\text{eV}$ on SiO_2 which matches with the literature. We also find lower Φ of SnS_2 ($\sim 3.6\text{eV}$) on MoTe_2 , which indicates charge transfer from MoTe_2 to SnS_2 .

S4. Linear I-V curves

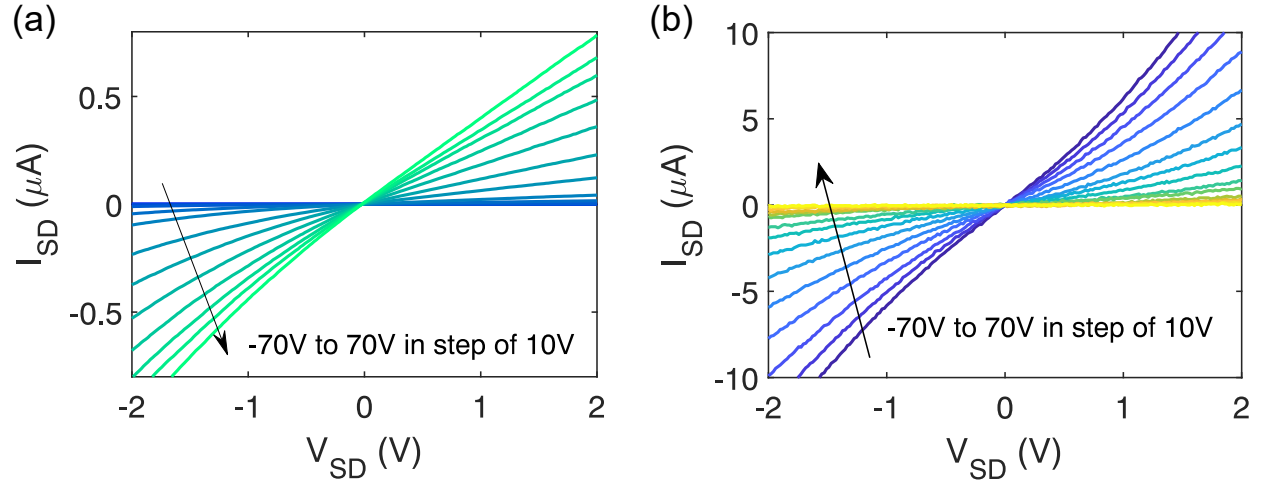


Figure S4: **Ohmic nature of the contacts:** (a) Output characteristics of SnS_2 and (b) MoTe_2 for $V_{SD} = -2\text{V}$ to $+2\text{V}$ for a range of backgate voltages showing linear behaviour.

Figure S4 (a) and (b) show the source-drain current (I_{SD}) vs. bias voltage (V_{SD}) applied across the individual flakes. The arrows show series of curves for a set of backgate voltages from -70V to 70V in the step of 10V, measured at 300K. For SnS_2 , the I_{SD} - V_{SD} curves are linear within $\pm 2\text{V}$. However, for MoTe_2 , the current tends to behave semi-linearly at higher bias voltages.

S5. Forward rectifying characteristics

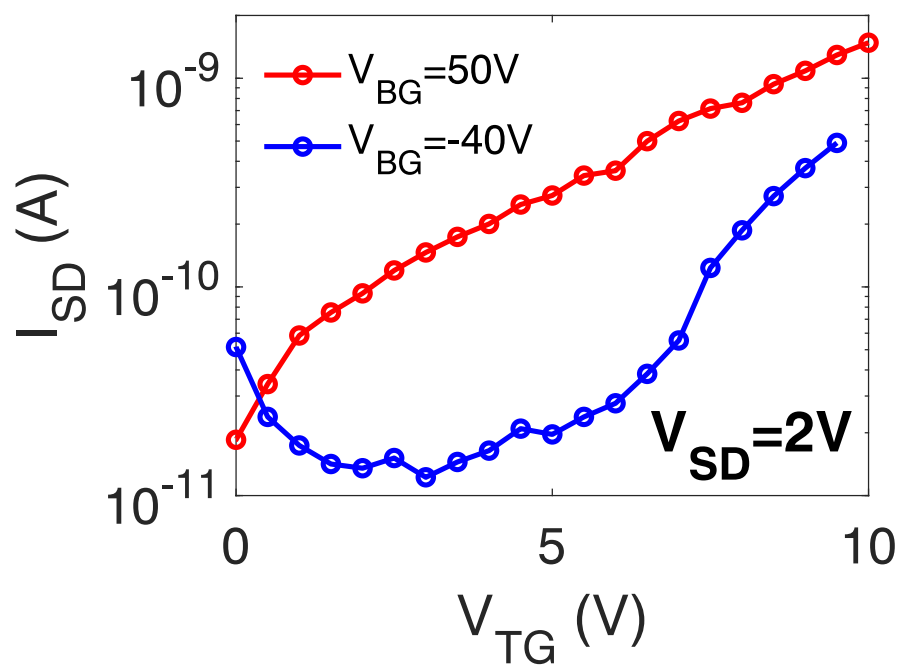


Figure S5: **Forward rectifying characteristics:** (a) I_{SD} vs V_{TG} plot for $V_{BG} = 50V$ and $-40V$ at $V_{SD} = 2V$ showing forward rectification.

S6. Calculation of Subthreshold swing from topgate response

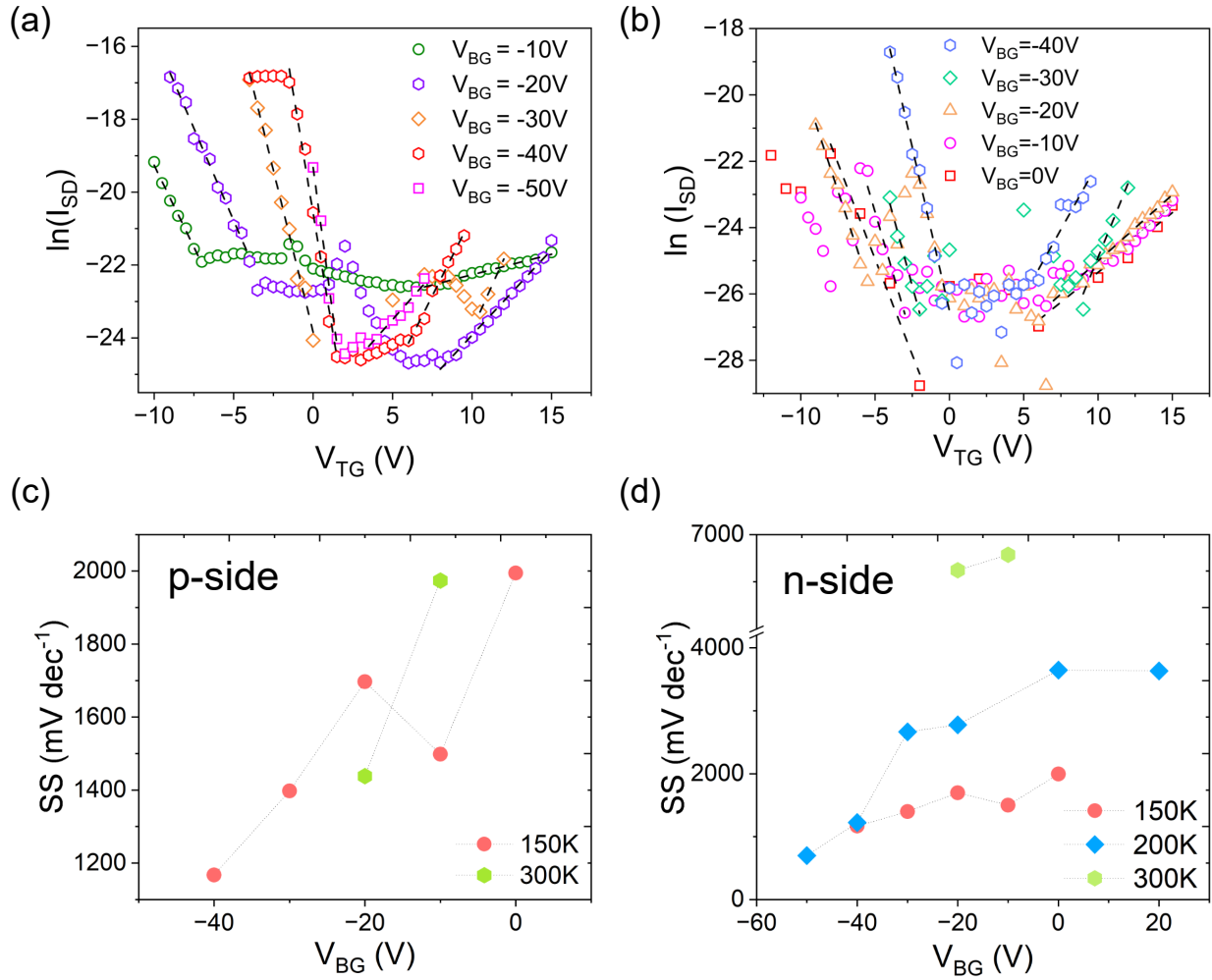


Figure S6: **Calculation of SS from the topgate response:** Plots of current $\ln(I_{SD})$ vs. topgate voltage V_{TG} for different backgate voltages at (a) $V_{SD} = 3V$ and (b) $V_{SD} = 0.5V$. The black dashed lines indicate linear fits. Sub-threshold swing (SS) vs. V_{BG} plotted at different temperatures for $V_{SD} = 0.5V$ for (c) p side and for (d) n side, calculated using equation S3.

Figure S6 shows junction current plotted in log scale $\ln(I_{SD})$ vs. V_{TG} for different backgate voltage at (a) $V_{SD} = 3V$ and (b) $0.5V$. We calculate the sub threshold swing (SS) from the topgate response of the junction. We use the following formula to calculate the sub-threshold

swing from the topgate response:

$$SS = \frac{\partial V_{\text{TG}}}{\partial(\log_{10} I_{\text{SD}})} = \log(10) \times \frac{\partial V_{\text{TG}}}{\partial(\ln I_{\text{SD}})} \quad (\text{S3})$$

The topgate response of the junction shows ambipolar response, showing both p and n-type conduction. Moreover, the sharper slope in the p-type conduction indicates different scattering mechanism responsible for the transport. We calculate SS for different temperatures for both p-side Fig. S6 (c) and n-side (d). These plot show SS having comparable values at 150K and 300K for the p-side. We find carrier transport to be dominant by tunneling in p-side as compared to n-side where the thermionic carrier injection is more prominent.

S7. Gate-tunable NDR at $V_{BG} = -50V$, 50K

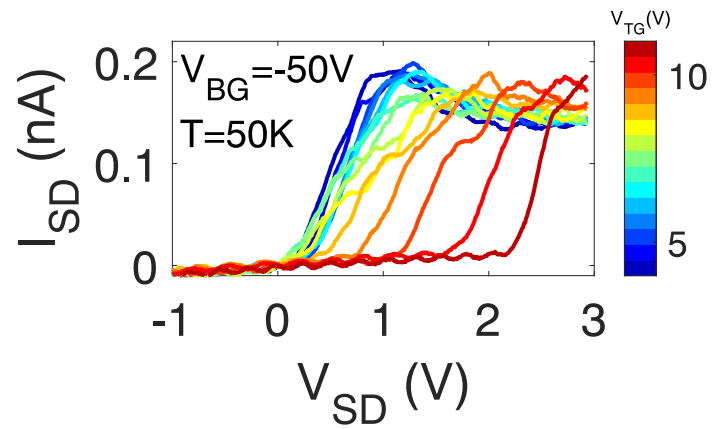


Figure S7: **Gate tunable NDR:** Topgate tunability of NDR signal observed in device D2 at $V_{BG} = -50V$ at 50K. This plot shows the NDR peak shifting towards higher bias at higher V_{TG} with negligible modulation in peak current.

S8. Back-gate tunability of NDR device D3

We present backgate tunability of NDR from a dual-gated device D3 at 300K and at 135K. Figure S8 (a), (b) and (c) show plots of I_{SD} vs. V_{SD} measured at 300K, 135K for $V_{TG} = 0V$, and at 135K for $V_{TG} = 2V$. We find gate-coupling efficiency to be $\eta \sim 0.12$ at 300K and ~ 0.08 at 135K, as shown in Fig. S8 (d). The lower η can be attributed to measurement resolution of backgate and thicker backgate dielectric of our devices. Fig. S8 (e) shows the peak current systematically changing with V_{BG} . We also show PVCR to be changing with V_{BG} upto a value ~ 4 as shown in Fig. S8 (f).

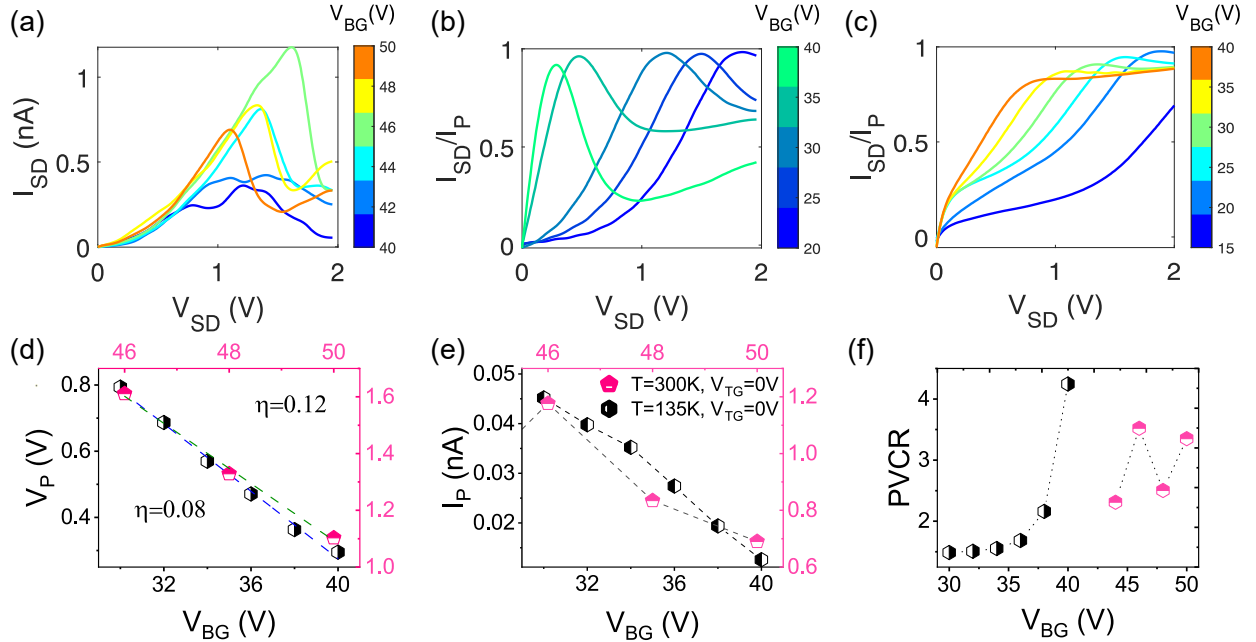


Figure S8: **Backgate tunability of NDR:** Source-drain current I_{SD} vs. bias voltage V_{SD} plots for range of backgate voltages showing the signature of negative differential resistance changing with V_{BG} at (a) 300K, $V_{TG} = 0V$ (b) 135K, $V_{TG} = 0V$ and (c) 135K, $V_{TG} = 2V$. (d) Gate-coupling efficiency (η) of NDR has been calculated by linear fitting V_P vs. V_{BG} plot for both 300K and 135K. Plots of peak current I_P vs. V_{BG} (e) and PVCR (f) are plotted at 300K and 135K.

S9. Inverse slope calculation

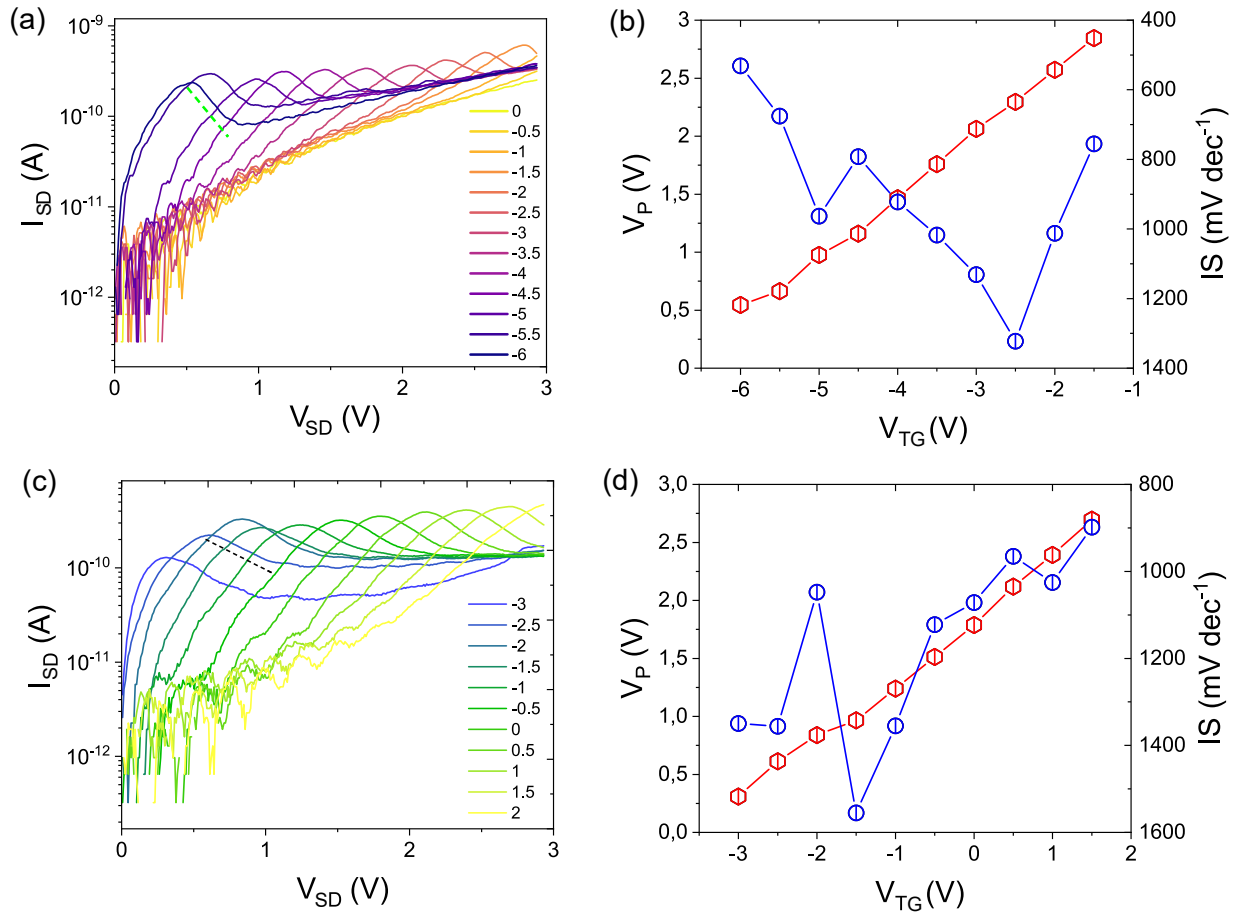


Figure S9: **Inverse slope:** Semi-log scale plot of I_{SD} with V_{SD} measured at $T=150K$ for $V_{BG} = -10V$ (a) and $-20V$ (c) for several topgate voltages. Inverse slope (IS) calculated from the slope as shown by the dashed lines. Topgate response of V_P (left axis) and IS (right axis) plotted together for $V_{BG} = -10V$ (b) and $-20V$ (d) respectively.

S10. Band structure calculation with different layer thickness

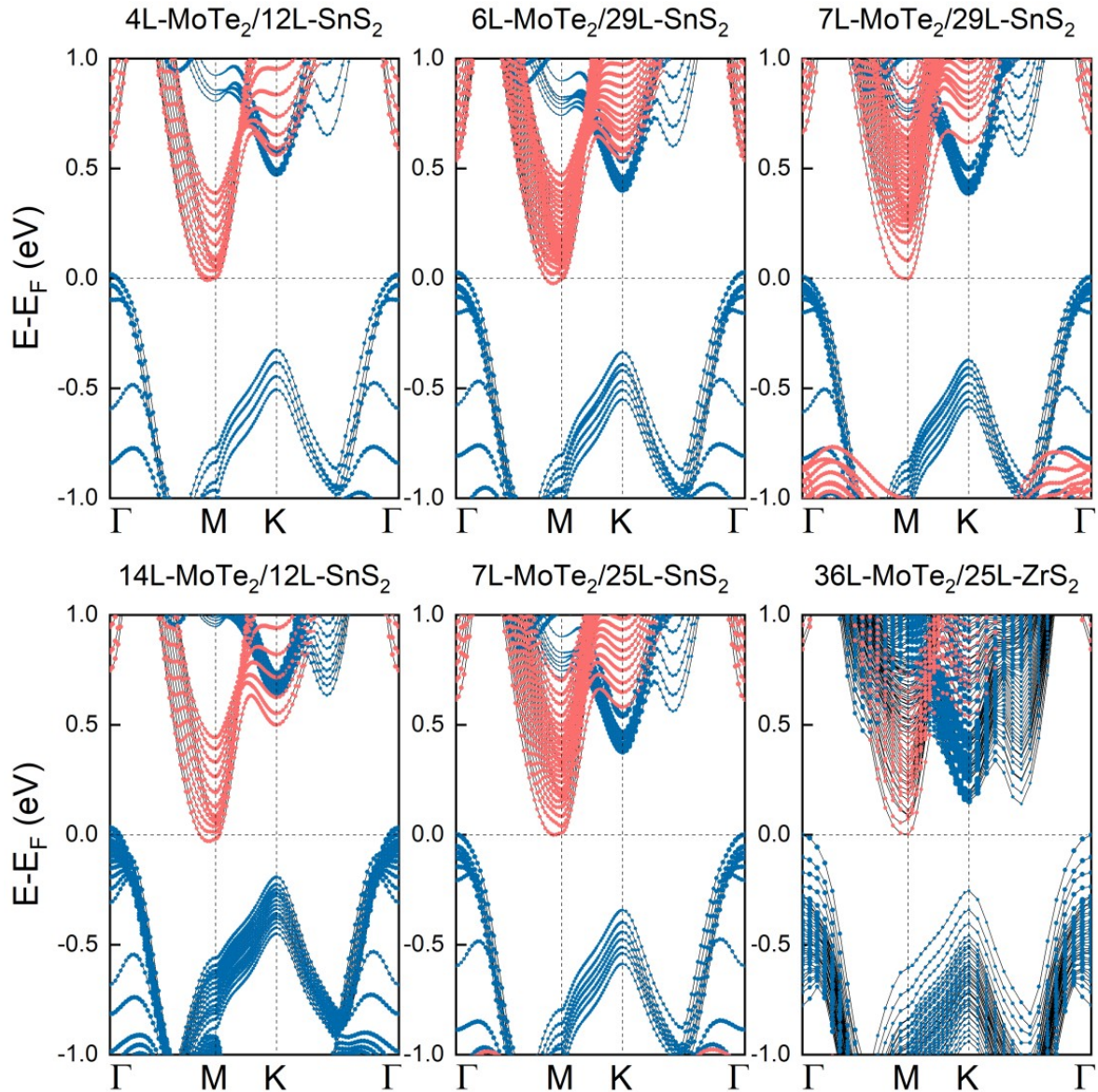


Figure S10: Band alignment of MoTe₂/SnS₂ heterostructure for different layer thicknesses. All the plots indicate nearly broken band alignment.

DFT simulations were carried out using the Vienna ab initio simulation package (VASP). The electron-ion interaction was described by PAW potentials with valence electron configurations of $4d^{10}5s^25p^2$ for Sn, $3s^23p^4$ for S, $4s^24p^64d^55s^1$ for Mo, and $5s^25p^4$ for Te. Periodic boundary conditions were applied and a vacuum space thicker than 15 \AA was included in the vertical direction to remove fictitious interactions between adjacent slabs. For both optimizations and electronic structure calculations van der Waals corrections were considered through the optB86b-vdW functional, and for all calculations the kinetic energy cutoff was set to 500 eV. Owing to the relatively low lattice mismatch between MoTe_2 and SnS_2 layers, heterostructures are built by simply stacking the corresponding unit cells. For our models, the strain is evenly shared within MoTe_2 and SnS_2 , and upon relaxations, both the atomic positions and the lattice constants are optimized. As a first step, we build heterostructures consisting of single-layer MoTe_2 and SnS_2 , with six high-symmetry stacking patterns. We find that the heterostructure for which top-layer S atoms are above Te atoms and bottom-layer S atoms are above Mo atoms, is the energetically favorable one. This stacking pattern is adopted for building thicker models, namely 4L- MoTe_2 /12L- SnS_2 , 6L- MoTe_2 /29L- SnS_2 , 7L- MoTe_2 /29L- SnS_2 , 14L- MoTe_2 /12L- SnS_2 , 7L- MoTe_2 /25L- SnS_2 , and 36L- MoTe_2 /25L- SnS_2 , which correspond to the experimentally observed thicknesses. Concerning the electronic properties, using standard DFT, we find that single-layer MoTe_2 is a semiconductor with a direct band gap of 1.14 eV, and by increasing the number of layers the band gap decreases. On the other hand, single-layer SnS_2 is an indirect gap semiconductor of 1.51 eV and smaller gaps are also observed for thicker SnS_2 layers. As shown in Fig. S10 all studied heterostructures exhibit the nearly broken gap band alignment which is promising for realizing tunneling transistors. Here we note that, for all studied heterostructures there is a small overlap between the high-lying valence states of MoTe_2 and the low-lying conduction states of SnS_2 apart from 36L- MoTe_2 /25L- SnS_2 heterostructure where a small effective gap is observed.

S11. Calculation of Tunnel current using DFT DOS

In this section we demonstrate the details of tunnel current (I_{Tunnel}) calculations from the density of states (DOS) extracted from the density functional theory (DFT). We base our modeling on the partial DOS of MoTe₂ and SnS₂ computed within DFT. Since DFT yields very good predictions of the shape of the DOS but often fails to reproduce the experimental band gaps of materials, we also apply a scissor shift to the calculated valence and conduction band to match experimental band gaps of 0.9 eV for bulk MoTe₂^{52,53} and 2.2 eV for bulk SnS₂⁵⁴ respectively. To study the effect of the size of the broken band gap, we also shift the DOS of the two materials in respect to each other and place the Fermi levels to match experimental observations of NDR in the present study.

Fig. S11 (a) and (b) show the equilibrium band alignment when (a) $E_{\text{Fm}} = E_{\text{Fs}} = -0.45$ eV with band overlap of 0 eV and (b) $E_{\text{Fm}} = E_{\text{Fs}} = -0.15$ eV with band overlap 0.6 eV. For all plots in this figure, $\text{DOS}_{\text{MoTe}_2}$ (blue curve) and $\text{DOS}_{\text{SnS}_2}$ (orange curve) plot with respect to energy with at equilibrium condition, for different band alignment conditions. For all our calculations, we use the DFT partial DOS of MoTe₂ and SnS₂ after the junction is formed. For all the plots at equilibrium, DOS in positive (negative) energy represents conduction (valence) band. Notably, the band alignment at zero overlap is defined as SnS₂ conduction band (CB) minima aligned with MoTe₂ valence band (VB) maxima. Positive (negative) band overlap is indicated as SnS₂ CB minima higher (lower) in energy with respect to MoTe₂ VB maxima. We use the following equation to calculate I_{Tunnel} :

$$I_{\text{Tunnel}} = \int_{E_{\text{Fm}}}^{E_{\text{Fs}}} \text{DOS}_{\text{MoTe}_2}(E) \times \text{DOS}_{\text{SnS}_2}(E - eV_{\text{Bias}}) \times [f_{\text{MoTe}_2}(E) - f_{\text{SnS}_2}(E - eV_{\text{Bias}})] dE \quad (\text{S4})$$

Here $\text{DOS}_{\text{MoTe}_2}$ ($\text{DOS}_{\text{SnS}_2}$) and f_{MoTe_2} (f_{SnS_2}) represent the DOS and the Fermi distribution function of MoTe₂ (SnS₂) respectively.

Fig. S11 (a), (c) show the band alignments of scenario (1) with $E_{\text{Fm}} = E_{\text{Fs}} = -0.45$ eV having a band overlap (or ‘gap’) of 0 eV for biasing conditions $V_{\text{Bias}} = 0\text{V}, 2.2\text{V}$ respectively.

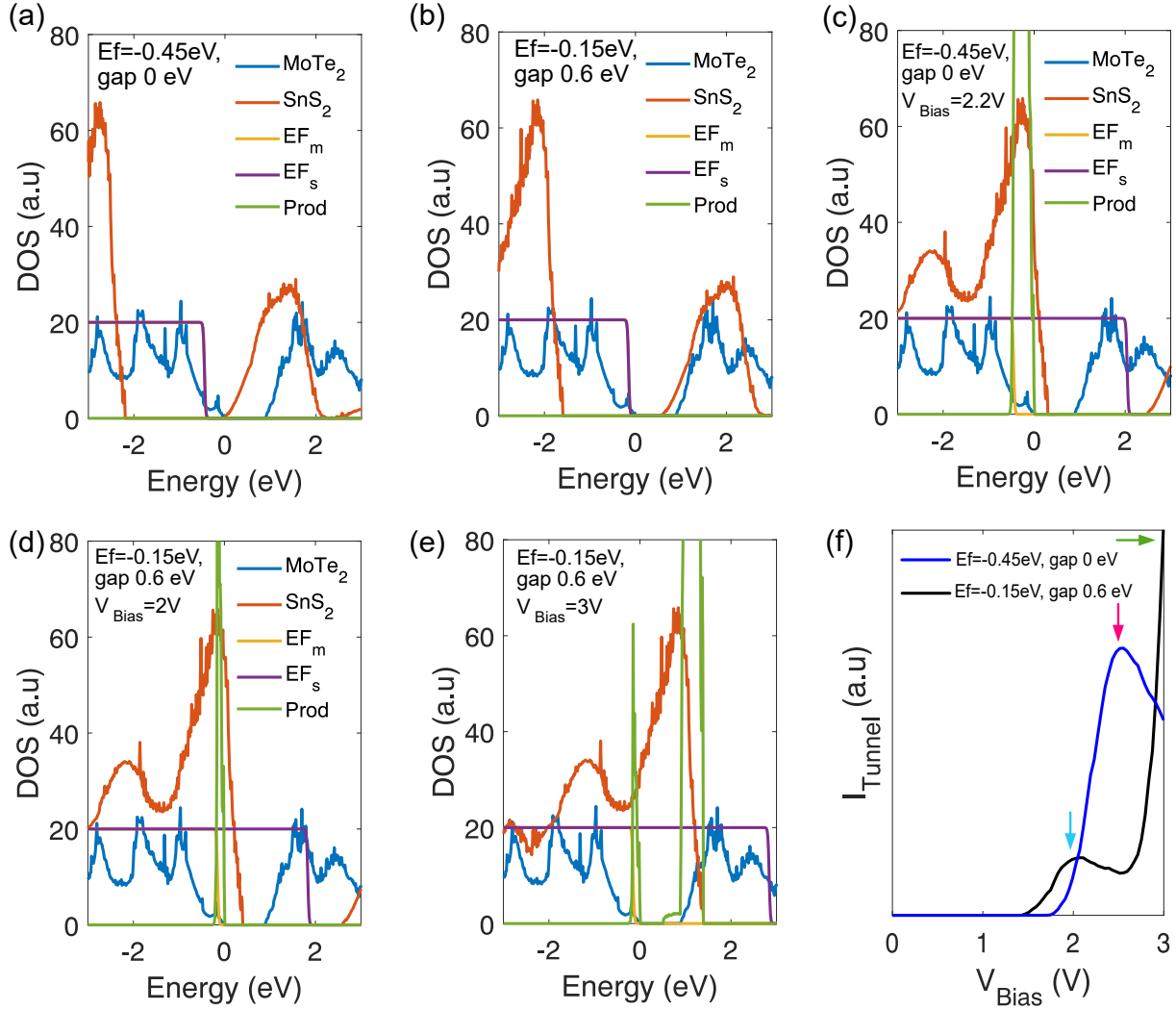


Figure S11: **Calculation of I_{Tunnel}** : Plots of partial DOS of MoTe₂ (blue), SnS₂ (orange), E_{Fm} (yellow), E_{Fs} (purple) and the integrand of the equation S4 (green) vs. energy for two equilibrium conditions ($V_{\text{Bias}} = 0\text{V}$) at (a) $E_{Fm} = E_{Fs} = -0.45\text{eV}$ with band overlap of 0 eV and (b) $E_{Fm} = E_{Fs} = -0.15\text{eV}$ with band overlap of 0.6 eV. Similar plots showing broken band alignment when bias voltage is applied, i.e. at (c) $E_{Fm} = E_{Fs} = -0.45\text{eV}$ with band overlap of 0 eV at 2.2V, and for $E_{Fm} = E_{Fs} = -0.15\text{eV}$ with band overlap of 0.6 eV at (d) 2V and (d) 3V. (f) I_{Tunnel} vs V_{Bias} plot for the mentioned scenarios. The colored arrows correspond to different bias voltages as shown in plot (c)-(e): red→(c), cyan→(d) and green→(e).

From these plots, we observe the integrand in eqn. S4, namely ‘product’ (green curves) to be non-zero at finite overlap of the bands which also depends on the positions of the Fermi energies of the two material. The integrated I-V curves are shown in Fig. S11 (f), where the colored arrow marks indicate the location of the bias voltages. Fig. S11 (c) and (d) show VB-VB tunneling to be contributing to the total current, whereas along with VB-VB, SnS₂ VB-MoTe₂ CB DOS overlap contribute at higher bias voltages as shown (e). Evidently this calculations indicate that, the dip in current appears when SnS₂ VB maxima aligns with the MoTe₂ bandgap. Fig. S11 (a) and (b) refer to band alignment schematic of pane I and III of Fig. 5(c). We refer to the situation when the Fermi energy is consistently changing with the band overlap and the NDR peak current modulates along with the peak position being shifted in bias voltages.

References

- (1) Liu, C.; Chen, H.; Wang, S.; Liu, Q.; Jiang, Y.-G.; Zhang, D. W.; Liu, M.; Zhou, P. Two-dimensional materials for next-generation computing technologies. *Nature Nanotechnology* **2020**, *15*, 545–557.
- (2) Ionescu, A. M.; Riel, H. Tunnel field-effect transistors as energy-efficient electronic switches. *nature* **2011**, *479*, 329–337.
- (3) Sarkar, D.; Xie, X.; Liu, W.; Cao, W.; Kang, J.; Gong, Y.; Kraemer, S.; Ajayan, P. M.; Banerjee, K. A subthermionic tunnel field-effect transistor with an atomically thin channel. *Nature* **2015**, *526*, 91–95.
- (4) Kanungo, S.; Ahmad, G.; Sahatiya, P.; Mukhopadhyay, A.; Chattopadhyay, S. 2D materials-based nanoscale tunneling field effect transistors: current developments and future prospects. *npj 2D Materials and Applications* **2022**, *6*, 83.

- (5) Boucart, K.; Ionescu, A. M. Double-gate tunnel FET with high- κ gate dielectric. *IEEE transactions on electron devices* **2007**, *54*, 1725–1733.
- (6) Nakamura, K.; Nagamura, N.; Ueno, K.; Taniguchi, T.; Watanabe, K.; Nagashio, K. All 2D heterostructure tunnel field-effect transistors: Impact of band alignment and heterointerface quality. *ACS Applied Materials & Interfaces* **2020**, *12*, 51598–51606.
- (7) Shim, J.; Oh, S.; Kang, D.-H.; Jo, S.-H.; Ali, M. H.; Choi, W.-Y.; Heo, K.; Jeon, J.; Lee, S.; Kim, M.; others Phosphorene/rhenium disulfide heterojunction-based negative differential resistance device for multi-valued logic. *Nature communications* **2016**, *7*, 13413.
- (8) Seo, S.; Cho, J.-I.; Jung, K.-S.; Andreev, M.; Lee, J.-H.; Ahn, H.; Jung, S.; Lee, T.; Kim, B.; Lee, S.; others A Van Der Waals Reconfigurable Multi-Valued Logic Device and Circuit Based on Tunable Negative-Differential-Resistance Phenomenon. *Advanced Materials* **2022**, *34*, 2202799.
- (9) Britnell, L.; Gorbachev, R.; Geim, A.; Ponomarenko, L.; Mishchenko, A.; Greenaway, M.; Fromhold, T.; Novoselov, K.; Eaves, L. Resonant tunnelling and negative differential conductance in graphene transistors. *Nature communications* **2013**, *4*, 1794.
- (10) Xiong, X.; Huang, M.; Hu, B.; Li, X.; Liu, F.; Li, S.; Tian, M.; Li, T.; Song, J.; Wu, Y. A transverse tunnelling field-effect transistor made from a van der Waals heterostructure. *Nature Electronics* **2020**, *3*, 106–112.
- (11) Seo, S.; Koo, J.; Choi, J.-W.; Heo, K.; Andreev, M.; Lee, J.-J.; Lee, J.-H.; Cho, J.-I.; Kim, H.; Yoo, G.; others Controllable potential barrier for multiple negative-differential-transconductance and its application to multi-valued logic computing. *npj 2D Materials and Applications* **2021**, *5*, 32.
- (12) Srivastava, P. K.; Hassan, Y.; de Sousa, D. J.; Gebredingle, Y.; Joe, M.; Ali, F.; Zheng, Y.; Yoo, W. J.; Ghosh, S.; Teherani, J. T.; others Resonant tunnelling diodes

- based on twisted black phosphorus homostructures. *Nature Electronics* **2021**, *4*, 269–276.
- (13) Jo, S. B.; Kang, J.; Cho, J. H. Recent advances on multivalued logic gates: a materials perspective. *Advanced Science* **2021**, *8*, 2004216.
- (14) Suleimenov, I. E.; Vitulyova, Y. S.; Kabdushev, S. B.; Bakirov, A. S. Improving the efficiency of using multivalued logic tools. *Scientific Reports* **2023**, *13*, 1108.
- (15) Bhattacharjee, D.; Kim, W.; Chattopadhyay, A.; Waser, R.; Rana, V. Multi-valued and fuzzy logic realization using TaOx memristive devices. *Scientific reports* **2018**, *8*, 8.
- (16) Chhowalla, M.; Jena, D.; Zhang, H. Two-dimensional semiconductors for transistors. *Nature Reviews Materials* **2016**, *1*, 1–15.
- (17) Liu, Y.; Duan, X.; Shin, H.-J.; Park, S.; Huang, Y.; Duan, X. Promises and prospects of two-dimensional transistors. *Nature* **2021**, *591*, 43–53.
- (18) Chaves, A.; Azadani, J. G.; Alsalman, H.; Da Costa, D.; Frisenda, R.; Chaves, A.; Song, S. H.; Kim, Y. D.; He, D.; Zhou, J.; others Bandgap engineering of two-dimensional semiconductor materials. *npj 2D Materials and Applications* **2020**, *4*, 29.
- (19) Bao, X.; Ou, Q.; Xu, Z.-Q.; Zhang, Y.; Bao, Q.; Zhang, H. Band structure engineering in 2D materials for optoelectronic applications. *Advanced Materials Technologies* **2018**, *3*, 1800072.
- (20) Hoque, M. A.; George, A.; Ramachandra, V.; Najafidehaghani, E.; Gan, Z.; Mitra, R.; Zhao, B.; Sahoo, S.; Abrahamsson, M.; Liang, Q.; others All-2D CVD-grown semiconductor field-effect transistors with van der Waals graphene contacts. *npj 2D Materials and Applications* **2024**, *8*, 55.
- (21) Roy, T.; Tosun, M.; Cao, X.; Fang, H.; Lien, D.-H.; Zhao, P.; Chen, Y.-Z.; Chueh, Y.-L.;

- Guo, J.; Javey, A. Dual-gated MoS₂/WSe₂ van der Waals tunnel diodes and transistors. *ACS nano* **2015**, *9*, 2071–2079.
- (22) Nourbakhsh, A.; Zubair, A.; Dresselhaus, M. S.; Palacios, T. Transport properties of a MoS₂/WSe₂ heterojunction transistor and its potential for application. *Nano letters* **2016**, *16*, 1359–1366.
- (23) Kim, J. H.; Sarkar, S.; Wang, Y.; Taniguchi, T.; Watanabe, K.; Chhowalla, M. Room Temperature Negative Differential Resistance with High Peak Current in MoS₂/WSe₂ Heterostructures. *Nano Letters* **2024**,
- (24) Lee, C.-H.; Lee, G.-H.; Van Der Zande, A. M.; Chen, W.; Li, Y.; Han, M.; Cui, X.; Arefe, G.; Nuckolls, C.; Heinz, T. F.; others Atomically thin p–n junctions with van der Waals heterointerfaces. *Nature nanotechnology* **2014**, *9*, 676–681.
- (25) Movva, H. C.; Kang, S.; Rai, A.; Kim, K.; Fallahazad, B.; Taniguchi, T.; Watanabe, K.; Tutuc, E.; Banerjee, S. K. Room temperature gate-tunable negative differential resistance in MoS₂/hBN/WSe₂ heterostructures. 2016 74th Annual Device Research Conference (DRC). 2016; pp 1–2.
- (26) Balaji, Y.; Smets, Q.; Szabo, Á.; Mascaro, M.; Lin, D.; Asselberghs, I.; Radu, I.; Luisier, M.; Groeseneken, G. MoS₂/MoTe₂ heterostructure tunnel FETs using gated Schottky contacts. *Advanced Functional Materials* **2020**, *30*, 1905970.
- (27) Yan, H.; Zhao, Q.; Chen, Y.; Wu, S.; Li, G.; Da, X.; Jiao, H.; Tai, X.; Xiao, Y.; Yan, S.; others MoTe₂/SnSe₂ Tunneling Diode Regulated by Giant Ferroelectric Field. *IEEE Transactions on Electron Devices* **2023**, *70*, 5966–5971.
- (28) Roy, T.; Tosun, M.; Hettick, M.; Ahn, G. H.; Hu, C.; Javey, A. 2D-2D tunneling field-effect transistors using WSe₂/SnSe₂ heterostructures. *Applied Physics Letters* **2016**, *108*.

- (29) Yan, X.; Liu, C.; Li, C.; Bao, W.; Ding, S.; Zhang, D. W.; Zhou, P. Tunable SnSe₂/WSe₂ heterostructure tunneling field effect transistor. *Small* **2017**, *13*, 1701478.
- (30) Oliva, N.; Backman, J.; Capua, L.; Cavalieri, M.; Luisier, M.; Ionescu, A. M. WSe₂/SnSe₂ vdW heterojunction Tunnel FET with subthermionic characteristic and MOSFET co-integrated on same WSe₂ flake. *npj 2D Materials and Applications* **2020**, *4*, 5.
- (31) Murali, K.; Dandu, M.; Das, S.; Majumdar, K. Gate-tunable WSe₂/SnSe₂ backward diode with ultrahigh-reverse rectification ratio. *ACS applied materials & interfaces* **2018**, *10*, 5657–5664.
- (32) Sato, Y.; Nishimura, T.; Duanfei, D.; Ueno, K.; Shinokita, K.; Matsuda, K.; Nagashio, K. Intrinsic electronic transport properties and carrier densities in PtS₂ and SnSe₂: exploration of n⁺-Source for 2D tunnel FETs. *Advanced Electronic Materials* **2021**, *7*, 2100292.
- (33) Guo, Z.; Hu, K.; Su, J.; Chen, J.; Dong, H.; Pan, M.; Nie, Z.; Wu, F. Tunable electronic properties and negative differential resistance effect of the intrinsic type-III ZrS₂/WTe₂ van der Waals heterostructure. *Applied Surface Science* **2023**, *611*, 155644.
- (34) Iordanidou, K.; Mitra, R.; Shetty, N.; Lara-Avila, S.; Dash, S.; Kubatkin, S.; Wiktor, J. Electric field and strain tuning of 2D semiconductor van der Waals heterostructures for tunnel field-effect transistors. *ACS Applied Materials & Interfaces* **2022**, *15*, 1762–1771.
- (35) Iordanidou, K.; Wiktor, J. Two-dimensional Mo Te₂/Sn Se₂ van der Waals heterostructures for tunnel-FET applications. *Physical Review Materials* **2022**, *6*, 084001.
- (36) Kim, S.; Du, H.; Kim, T.; Shin, S.; Song, H.-k.; Kim, H.; Kang, D.; Lee, C.-W.; Seo, S. Gate-switchable rectification in isotype van der Waals heterostructure of multilayer MoTe₂/SnS₂ with large band offsets. *npj 2D Materials and Applications* **2020**, *4*, 15.

- (37) Chen, C.-F.; Yang, S.-H.; Lin, C.-Y.; Lee, M.-P.; Tsai, M.-Y.; Yang, F.-S.; Chang, Y.-M.; Li, M.; Lee, K.-C.; Ueno, K.; others Reversible Charge-Polarity Control for Multioperation-Mode Transistors Based on van der Waals Heterostructures. *Advanced Science* **2022**, *9*, 2106016.
- (38) Li, A.; Chen, Q.; Wang, P.; Gan, Y.; Qi, T.; Wang, P.; Tang, F.; Wu, J. Z.; Chen, R.; Zhang, L.; others Ultrahigh-sensitive broadband photodetectors based on dielectric shielded MoTe₂/Graphene/SnS₂ p-g-n junctions. *Advanced Materials* **2019**, *31*, 1805656.
- (39) Wu, F.; Tian, H.; Yan, Z.; Ren, J.; Hirtz, T.; Gou, G.; Shen, Y.; Yang, Y.; Ren, T.-L. Gate-tunable negative differential resistance behaviors in a hBN-Encapsulated BP-MoS₂ Heterojunction. *ACS Applied Materials & Interfaces* **2021**, *13*, 26161–26169.
- (40) Mahajan, M.; Majumdar, K. Gate-and light-tunable negative differential resistance with high peak current density in 1T-TaS₂/2H-MoS₂ T-junction. *ACS nano* **2020**, *14*, 6803–6811.
- (41) Fan, S.; Vu, Q. A.; Lee, S.; Phan, T. L.; Han, G.; Kim, Y.-M.; Yu, W. J.; Lee, Y. H. Tunable negative differential resistance in van der Waals heterostructures at room temperature by tailoring the interface. *ACS nano* **2019**, *13*, 8193–8201.
- (42) Fallahazad, B.; Lee, K.; Kang, S.; Xue, J.; Larentis, S.; Corbet, C.; Kim, K.; Movva, H. C.; Taniguchi, T.; Watanabe, K.; others Gate-tunable resonant tunneling in double bilayer graphene heterostructures. *Nano letters* **2015**, *15*, 428–433.
- (43) Yan, R.; Fathipour, S.; Han, Y.; Song, B.; Xiao, S.; Li, M.; Ma, N.; Protasenko, V.; Muller, D. A.; Jena, D.; others Esaki diodes in van der Waals heterojunctions with broken-gap energy band alignment. *Nano letters* **2015**, *15*, 5791–5798.
- (44) Srivastava, P. K.; Hassan, Y.; Gebredingle, Y.; Jung, J.; Kang, B.; Yoo, W. J.; Singh, B.;

- Lee, C. Multifunctional van der Waals broken-gap heterojunction. *Small* **2019**, *15*, 1804885.
- (45) Xiao, S.; Zheng, T.; Chen, W.; Zhang, J.; Yang, M.; Sun, Y.; Zheng, Z.; Hao, D.; Huo, N.; Chen, Z.; others Multifunctional Phototransistor Based on Double Van der Waals Heterojunction with Reversed Band Edge Bending. *Advanced Functional Materials* **2024**, 2403509.
- (46) Jain, A.; Bharadwaj, P.; Heeg, S.; Parzefall, M.; Taniguchi, T.; Watanabe, K.; Novotny, L. Minimizing residues and strain in 2D materials transferred from PDMS. *Nanotechnology* **2018**, *29*, 265203.
- (47) Kim, C.; Moon, I.; Lee, D.; Choi, M. S.; Ahmed, F.; Nam, S.; Cho, Y.; Shin, H.-J.; Park, S.; Yoo, W. J. Fermi level pinning at electrical metal contacts of monolayer molybdenum dichalcogenides. *ACS nano* **2017**, *11*, 1588–1596.
- (48) Aftab, S.; Iqbal, M. W.; Afzal, A. M.; Khan, M. F.; Hussain, G.; Waheed, H. S.; Kamran, M. A. Formation of an MoTe₂ based Schottky junction employing ultra-low and high resistive metal contacts. *RSC advances* **2019**, *9*, 10017–10023.
- (49) Lv, C.; Yan, W.; Shieh, T.-H.; Zhao, Y.; Wu, G.; Zhao, Y.; Lv, Y.; Zhang, D.; Chen, Y.; Arora, S. K.; others Electrical contact barriers between a three-dimensional metal and layered SnS₂. *ACS applied materials & interfaces* **2020**, *12*, 15830–15836.
- (50) Sriv, T.; Kim, K.; Cheong, H. Low-frequency Raman spectroscopy of few-layer 2H-SnS₂. *Scientific Reports* **2018**, *8*, 10194.
- (51) Fraser, J. P.; Masaityte, L.; Zhang, J.; Laing, S.; Moreno-López, J. C.; McKenzie, A. F.; McGlynn, J. C.; Panchal, V.; Graham, D.; Kazakova, O.; others Selective phase growth and precise-layer control in MoTe₂. *Communications Materials* **2020**, *1*, 48.

- (52) Ruppert, C.; Aslan, B.; Heinz, T. F. Optical properties and band gap of single-and few-layer MoTe₂ crystals. *Nano letters* **2014**, *14*, 6231–6236.
- (53) Koo, B.; Shin, G. H.; Park, H.; Kim, H.; Choi, S.-Y. Vertical-tunneling field-effect transistor based on MoTe₂/MoS₂ 2D–2D heterojunction. *Journal of Physics D: Applied Physics* **2018**, *51*, 475101.
- (54) Schlaf, R.; Lang, O.; Pettenkofer, C.; Jaegermann, W. Band lineup of layered semiconductor heterointerfaces prepared by van der Waals epitaxy: Charge transfer correction term for the electron affinity rule. *Journal of applied physics* **1999**, *85*, 2732–2753.